

A hydrodynamical study of multiple-shell planetary nebulae

III. Expansion properties and internal kinematics: Theory versus observation*

D. Schönberner^{1, **}, R. Jacob¹, H. Lehmann², G. Hildebrandt^{1, °}, M. Steffen¹, A. Zwanzig¹, C. Sandin¹, and R.L.M. Corradi^{3, 4}

¹ Leibniz-Institut für Astrophysik Potsdam, An der Sternwarte 16, D-14482 Potsdam, Germany

² Thüringer Landessternwarte Tautenburg, Karl-Schwarzschild-Observatorium, D-07778 Tautenburg, Germany

³ Instituto de Astrofísica de Canarias, E-38200 La Laguna, Tenerife, Spain

⁴ Departamento de Astrofísica, Universidad de La Laguna, E-38206 La Laguna, Tenerife, Spain

Received 2014 Feb 3, accepted 2014 Mar 7

Published online 2014 May 2

Key words hydrodynamics – lines: profiles – planetary nebulae: general – techniques: spectroscopic

We present the result of a study on the expansion properties and internal kinematics of round/elliptical planetary nebulae of the Milky Way disk, the halo, and of the globular cluster M 15. The purpose of this study is to considerably enlarge the small sample of nebulae with precisely determined expansion properties (Schönberner et al. 2005b). To this aim, we selected a representative sample of objects with different evolutionary stages and metallicities and conducted high-resolution échelle spectroscopy. In most cases we succeeded in detecting the weak signals from the outer nebular shell which are attached to the main line emission from the bright nebular rim. Next to the measurement of the motion of the rim gas by decomposition the main line components into Gaussians, we were able to measure separately, for most objects for the first time, the gas velocity immediately behind the leading shock of the shell, i.e. the post-shock velocity. We more than doubled the number of objects for which the velocities of both rim and shell are known and confirm that the overall expansion of planetary nebulae is accelerating with time. There are, however, differences between the expansion behaviour of the shell and the rim: The post-shock velocity is starting at values as low as around 20 km s^{-1} for the youngest nebulae, just above the AGB wind velocity of $\sim 10\text{--}15 \text{ km s}^{-1}$, and is reaching values of about 40 km s^{-1} for the nebulae around hotter central stars. Contrarily, the rim matter is at first decelerated below the typical AGB-wind velocity and remains at about $5\text{--}10 \text{ km s}^{-1}$ for a while until finally a typical flow velocity of up to 30 km s^{-1} is reached. This observed distinct velocity evolution of both rim and shell is explained by radiation-hydrodynamics simulations, at least qualitatively: It is due to the ever changing stellar radiation field and wind-wind interaction together with the varying density profile ahead of the leading shock during the progress of evolution. The wind-wind interaction works on the rim dynamics while the radiation field and upstream density gradient is responsible for the shell dynamics. Because of these time-dependent boundary conditions, a planetary nebula will never evolve into a simple self-similar expansion. Also the metal-poor objects behave as theory predicts: The post-shock velocities are higher and the rim flow velocities are equal or even lower compared to disk objects at similar evolutionary stage. The old nebula around low-luminosity central stars contained in our sample expand still fast and are dominated by reionisation. We detected, for the first time, in some objects an asymmetric expansion behaviour: The relative expansions between rim and shell appear to be different for the receding and approaching parts of the nebular envelope.

© 2014 WILEY-VCH Verlag GmbH & Co. KGaA, Weinheim

1 Introduction

1.1 Historical background

The process of formation and evolution of planetary nebulae (PNe) is intimately connected with mass-loss processes along the asymptotic giant branch (AGB) and the final contraction and heating of the stellar remnant until the white-dwarf cooling path at the hot side of the Hertzsprung-

Russell diagram (HRD) is reached. Thereby, the slow but very dense AGB wind is heated by photo-ionisation due to the intense radiation field of the hot central star and compressed from within by the action of the tenuous but very fast central-star wind.

There is, however, no direct interaction of the fast wind with the former AGB matter: The wind is thermalised by a strong shock, and the system's steady attempt to achieve pressure balance between the ionised shell and this shocked wind material on one side, and between the shell and the still undisturbed AGB wind on the other side is responsible for the formation of what we call a planetary nebula and its evolution with time. In this view a PN is not sim-

* Based partly on observations obtained at the European Southern Observatory, Paranal, Chile (ESO programme No. 077.D-0652).

** Corresponding author: deschoenberner@aip.de

° Deceased on 2004 December 23.

ply the evidence of matter ejected from the stellar surface but can instead be described by a thermally driven shock wave through the ambient AGB wind envelope, starting at the inner edge of this envelope and powered by heating due to photo-ionisation. Morphology and kinematics of PNe are thus the result of shock waves initiated by ionisation and modified by winds interaction, and their physics may not be described adequately by static models.

The expansion of a PN is usually measured by the Doppler split components (if the line is resolved) or the line width (if unresolved) of strong emission lines. Since the pioneering work of Wilson (1950) it is known that the velocity field within a planetary nebula is not uniform. Instead, one has to assume that the flow velocity generally increases with distance from the central star. Because of this (positive) velocity gradient, lines of ions with different ionisation potential exhibit different line splits if the ionisation within the nebular shell is stratified.

Although already known from photographic images, observations with modern, sensitive CCD detectors revealed many more PNe which consist of up to three distinct shells. The inner two shells make up the PN proper, and Frank, Balick & Riley (1990) coined the terms “rim” for the inner, bright shell and “shell” for the outer one which is usually fainter. The rim encloses an inner cavity containing the hot shocked wind gas from the central star. The third, extremely faint but mostly round region which embraces the shell is called “halo” and consists of the ionised AGB wind. A recent compilation of PNe with detected halos is those of Corradi et al. (2003), but see also Frew, Bojičić & Parker (2012). An example for the typical morphology of a multiple-shell PN is rendered in Fig. 1. Since we are dealing with the two main nebular shells only, we use also the term “double-shell” planetary in the following.

While the density structure can be deduced from monochromatic images, the velocity field requires high-resolution spectroscopy of the emission lines, and the interpretation in terms of the internal velocity field is anything but straightforward. One reason is intrinsic to the objects: Density structure and velocity field are intertwined such that a measured line split along the central line-of-sight probes the matter velocity at a radial position corresponding to the largest emission measure, or more precisely, from the line split one derives only an average velocity, where the average along the line-of-sight is weighted by density squared. The other reason is that normally the emission from the shell is rather weak and escapes detection in spectrograms of poor quality. This is very unfortunate since the shell contains usually most and the fastest moving matter of the whole object!

According to Chu, Jacoby & Arendt (1987), at least 50% of all round/elliptical PNe appear to be of the multiple-shell (or double-shell) type. By means of high-resolution échelle spectrograms, Chu et al. (1984) and Chu (1989) detected also the typical spectroscopic signatures of the shell as weak (outer) shoulders attached to the main emission-line profile originating from the bright rim and noted that there

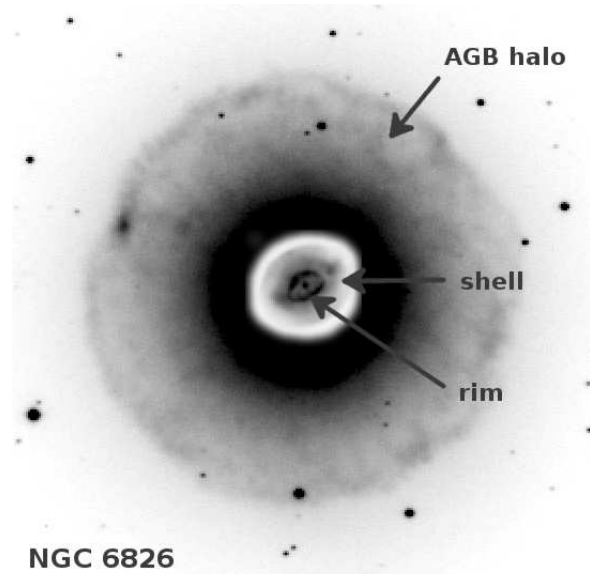


Fig. 1 Combination of two [O III] images of the multiple-shell planetary nebula NGC 6826 with different (logarithmic) intensity scales for inset and main image (see Corradi et al. 2003 for details). The inset picture shows the PN proper, consisting of rim and shell. The nebula is expanding into the rather large, only slowly expanding spherical halo consisting of ionised AGB-wind matter.

are obviously two different expansion modes one has to deal with. Normally, the shell is faster than the rim, but exceptions are also known (cf. Sabbadin et al. 1984). A good example for normal expansion is the well-known PN NGC 6826 where Chu et al. (1984) deduced an expansion velocity of 27 km s^{-1} for the shell from the outer, weak shoulders of the line profile, in contrast to 8 km s^{-1} for the rim from the strong, doubly peaked central profile components (cf. also our Fig. 7 in Sect. 2.1).

Important more recent observational studies concerning the structure and kinematics of PNe, partly employing (static) nebula models together with high-resolution line profiles, are those of Stanghellini & Pasquali (1995) (only structure), Gesicki, Acker & Szczerba (1996), Gesicki et al. (1998), Guerrero, Villaver & Manchado (1998), Gesicki & Zijlstra (2000) (only kinematics), Neiner et al. (2000), and Gesicki, Acker & Zijlstra (2003). Especially interesting is the study by Sabbadin et al. (2004) on NGC 7009 in which two distinct velocity laws for rim and shell could be derived.

All these studies agree upon the facts that

1. the expansion velocity does not necessarily increase linearly with distance from the central star, and that
2. often the gas velocity reaches a local minimum roughly at the rim/shell interface, i.e. rim and shell have very distinct expansion behaviours, and usually the shell matter reaches the highest expansion velocities.

One can conclude from these studies that planetary nebulae *do not* expand according to a $v(r) \propto r$ law, although this assumption is still often used to construct spatiokinematical

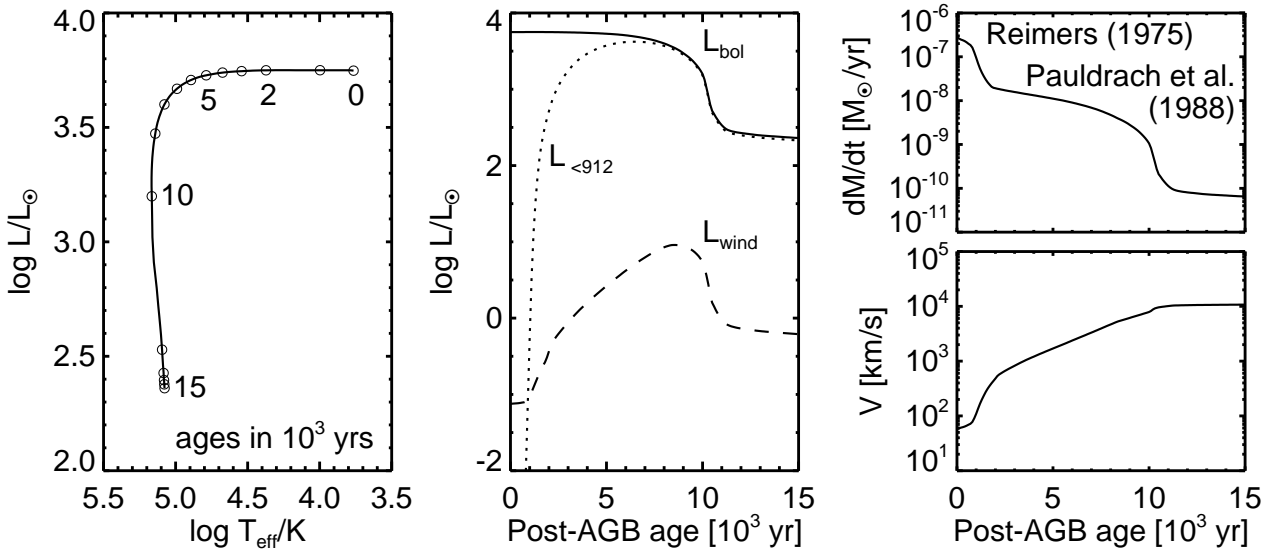


Fig. 2 Example of stellar and wind properties used in our simulations as inner boundary conditions. *Left panel:* evolutionary path for a 0.595 M_⊙ post-AGB model with the post-AGB ages ages indicated; *middle panel:* the corresponding time evolution of the bolometric, L_{bol} (solid), Lyman continuum, $L_{<912}$ (dotted), and mechanical (wind) luminosity, $L_{\text{wind}} = \dot{M} V^2/2$ (dashed), all in units of L_{\odot} . *Right panels:* mass-loss rate \dot{M} (top) and wind velocity V (bottom). The end of the strong AGB wind sets the zero point of the post-AGB evolution and the beginning of the much weaker post-AGB wind, modelled first by the prescription of Reimers (1975). Later, for $T_{\text{eff}} \geq 25\,000$ K, or post-AGB ages $\geq 2 \times 10^3$ years, the theory of radiation-driven winds as formulated by Pauldrach et al. (1988) is used for the rest of the evolution.

models (but see also Steffen & López 2006; Steffen, García Segura & Koning 2009).

It has early been realised that deciphering the expansion behaviour of PNe is important for understanding their formation and evolution. For instance, the total lifetime, or visibility time, of PNe is an important quantity to determine the total PN number of a stellar population, either by observations or theoretically by stellar population synthesis calculation (cf. Moe & de Marco 2006). This, however, is an uncertain endeavour as long as the internal kinematics and especially the “true” expansion velocity of PNe is not known. A recent discussion of this subject can be found in Jacob, Schönberner & Steffen (2013).

Also, the problem of individual distances is an obstacle if observed peak line separations or line half widths are plotted against nebular radii, i.e. if one wants to deduce any evolution of the expansion with time. From the early works of Bohuski & Smith (1974) and Robinson et al. (1982) a certain trend of “expansion” velocities with radii is detectable (see, e.g., Fig. 2 in Bianchi 1992 for a more recent study of this kind), but the only safe statement one can make is that PNe start their evolution with comparably low expansion rates. How and why this expansion increases with time remained quite obscure. These analyses were additionally hampered by the fact that no distinction regarding nebular morphology and/or central-star type (Wolf-Rayet vs. O-type) was made.

The first convincing observational evidence about the increase of nebular expansion rates (as measured from half widths of strong emission lines) with time or evolution was

presented by Dopita & Meatheringham (1991) for Magellanic Clouds PNe and by Méndez, Kudritzki & Herrero (1992) for Milky Way objects. In both studies a systematic increase of the emission line widths with stellar temperature was found, based on the (distance-independent) central-star temperatures as a proxy of evolution.

Medina et al. (2006) discriminated, for the first time, between WR and normal spectral types of the central stars and found indications that nebula around WR central stars expand faster than those around O-type central stars. Dopita & Meatheringham (1991) and also Medina et al. (2006) used the 10% level of the line profile in order to get hold of the fastest expanding matter. Richer et al. (2008, 2010) studied the kinematics of PNe of the Milky Way bulge and found also that the HWHM velocities increase with the pace of evolution. These authors used various distance-independent indicators to discriminate the evolutionary states, as, e.g., the strength of He II $\lambda 4686$ Å.

1.2 Theoretical considerations

Radiation-hydrodynamics simulations provide a rather detailed picture how a PN is being formed (see, e.g., Schmidt-Voigt & Köppen 1987a, 1987b; Marten & Schönberner 1991; Mellema 1994, 1995; Villaver et al. 2002; Perinotto et al. 2004): Ionisation creates a rarefaction wave (the shell) which expands into the ambient medium (the former AGB wind), led by a shock. The innermost, only very slowly expanding part of this wave is being compressed and accelerated into a dense rim by the (thermal) pressure of the so-

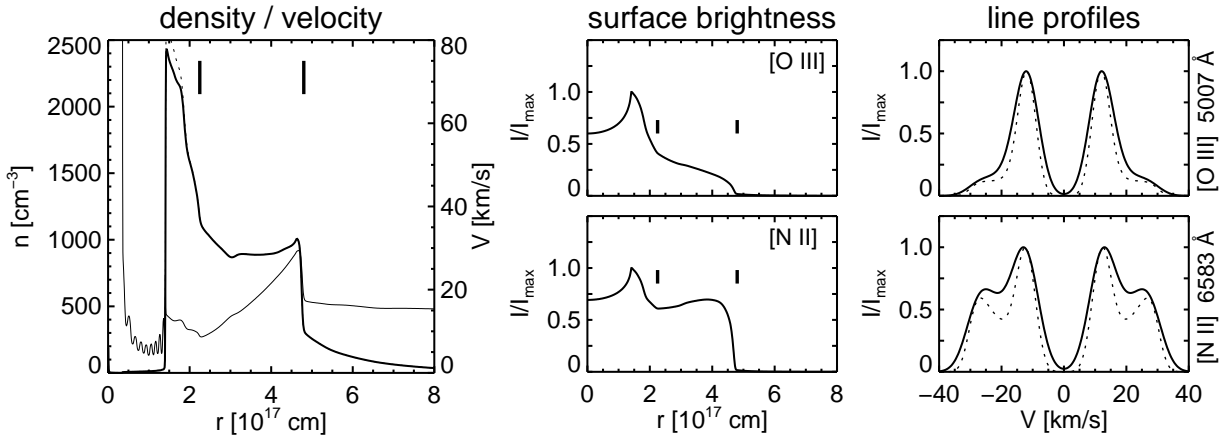


Fig. 3 Snapshot of a typical middle-aged nebular model from a 1D-radiation-hydrodynamics simulation around a $0.595 M_{\odot}$ central star whose properties are shown in Fig. 2 (cf. Schönberner et al. 2005a). The stellar parameters are: post-AGB age $t = 6106$ yr, $T_{\text{eff}} = 80177$ K, and $L = 5.057 \times 10^3 L_{\odot}$. *Left panel*: heavy particle density (thick), electron density (dotted), and gas velocity (thin); *middle panels*: (normalised) surface brightnesses in [O III] $\lambda 5007$ Å and [N II] $\lambda 6583$ Å; *right panels*: the corresponding normalised line profiles computed for the central line-of-sight with infinite spectral resolution (dotted) and broadened with a Gaussian of 6 km s^{-1} FWHM (solid), both with a circular aperture of 1×10^{16} cm. The thick vertical marks (*left and middle*) indicate the positions of the leading shocks of the rim and shell, respectively. The nebular mass enclosed by the rim’s shock is $M_{\text{rim}} = 0.07 M_{\odot}$, that enclosed by the shell’s leading shock is $M_{\text{shell}} = 0.47 M_{\odot}$ (= total nebular mass).

called “hot bubble” which consists of wind matter from the central star heated to very high temperatures ($\approx 10^6$ – 10^7 K) by the reverse wind shock and is separated from the nebula proper by a contact discontinuity.¹ Kinematics and shape of the wind-compressed rim is controlled by the wind power of the central star and the density and velocity of the ambient medium, which is here given by the low-velocity inner tail of the shell (Koo & McKee 1992). In contrast, the propagation speed of the shell’s shock, \dot{R}_{out} , is exclusively determined by the electron temperature ($\dot{R}_{\text{out}} \propto \sqrt{T_e}$) and the upstream density gradient (Franco, Tenorio-Tagle & Bodenheimer 1990; Chevalier 1997; Shu et al. 2002).

Thus, the typical PN consists, next to the hot bubble which is only seen in X-rays, of two important dynamical subsystems, the shell and the rim. In the simplest case of a spherical configuration, morphology and kinematics are ruled by (i) the radial run of the density gradient of the ambient matter together with a changing nebular electron temperature, and (ii) the evolution of stellar wind power and radiation field with time. This means that the kinematics of shell and rim are expected to be quite independent of each other: The shell’s expansion depends mainly on the previous mass-loss rate variation along the tip of the AGB because the electron temperature increases only slowly with evolution, while the expansion of the rim depends mainly on the

stellar wind evolution and, to a lesser extend, on the shell’s expansion properties.

As the shell’s shock expands faster than the rim, the shell becomes diluted while at the same time the slowly moving rim becomes much denser and brighter: the typical double-shell structure emerges very soon. The real expansion speed of a PN is, of course, defined by the propagation of the shell’s leading shock, but this velocity cannot be measured spectroscopically! For more details, see Schönberner et al. (2005a, 2005b, 2010).

During its expansion, a PN “sees” orders of magnitude changes of the stellar UV-radiation field and the wind power. An illustration is given in Fig. 2 for a $0.595 M_{\odot}$ post-AGB model where the changes of important stellar quantities are displayed: luminosities of the UV radiation and the wind (middle panel), mass-loss rate and wind velocity (right panel).²

Noticeable is the following: While the power of the UV-radiation field increases rapidly with time (and effective temperature), the wind power increases more gradually with time from a value as low as $\approx 10^{-4} L_{\text{bol}}$ to a maximum value of about $\approx 10^{-2.5} L_{\text{bol}}$ at the end of the horizontal part of evolution through the HRD, at about maximum stellar temperature. This increase of the wind power is entirely due to the growing wind speed as the star shrinks, which more

¹ Mellema (1995) used a different notation: The rim is called “W-shell” (W = wind) because it is the signature of interactions between the fast stellar wind and the older, slowly expanding former AGB material, and our shell is named “I-shell” (I = ionisation) because it is originally generated by ionisation. Consequently, the rim is bounded by a “W-shock”, and the shell by an “I-shock”.

² All model sequences shown in this work are based on the NEBEL code whose physical and numerical details are described in Perinotto et al. (1998). The atomic data used for the (time-dependent) ionisation/recombination calculations are listed in Marten & Szczerba (1997). An update of these data has only a negligible influence on the hydrodynamical properties of the models and is not necessary as long as one is not interested in the determination of chemical abundances.

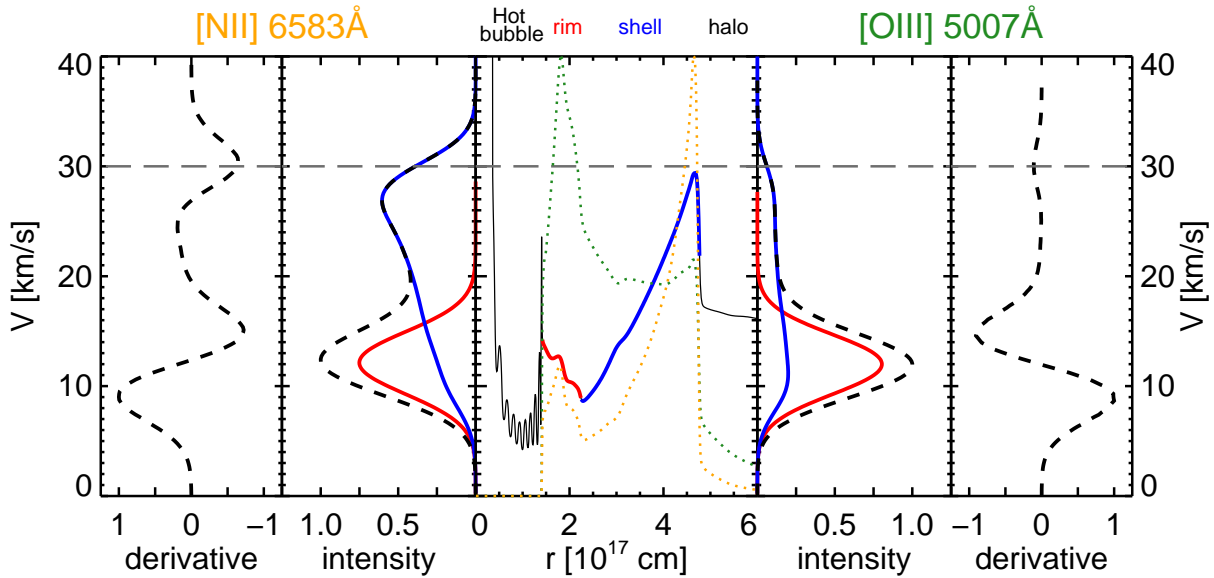


Fig. 4 Receding-shell components of the normalised lines [N II] $\lambda 6583 \text{ \AA}$ (next to left) and [O III] line $\lambda 5007 \text{ \AA}$ (next to right), computed (black dashed) for the model nebula shown in the middle panel and decomposed into the different contributions of rim (red) and shell (blue). The model is the same as displayed in Fig. 3, but here we render the velocity profile only (thick solid red and blue), supplemented by the normalised densities of N^+ (orange dotted) and O^{++} (green dotted). Thin lines indicate the velocity field belonging to the hot bubble and the halo. Both the outermost panels display the derivatives of both line profiles. The (relative) minima which belong to the profiles' inflection points at 30 km s^{-1} are marked by the horizontal dashed line. The value of the model's post-shock velocity is 29.5 km s^{-1} .

than compensates for the decrease of the mass-loss rate: from typical AGB-wind velocities up to $10\,000 \text{ km s}^{-1}$ at the white-dwarf stage. Only beyond maximum stellar temperature we see a rapid decline of the wind power in parallel with the drop of stellar luminosity while the wind speed remains constant.

The low wind power at the beginning suggests that formation and early shaping of PNe is mainly ruled by photoionisation and not by interacting winds, as is the general assumption in the literature. The effect of photoionisation becomes even more important in systems with low metallicity, hence also with weaker winds, as demonstrated by Schönberner et al. (2010).

An illustration of the typical nebular structure and the corresponding observable quantities like radial intensity and line profiles that are predicted by 1D-hydrodynamical simulations is rendered in Fig. 3. This particular model belongs to a radiation-hydrodynamics PN simulation around a $0.595 M_{\odot}$ central star whose properties are illustrated in Fig. 2. The initial shell configuration is based on hydrodynamical simulations of dusty AGB envelopes during the final AGB evolution (see Steffen et al. 1998 for details). Theoretical line profiles are computed for central lines of sight with a numerical aperture of $1 \times 10^{16} \text{ cm}$ radius, broadened by a Gaussian of FWHM of 6 km s^{-1} to mimick a typical finite spectral resolution. More details about this particular sequence can be seen in Schönberner et al. (2005a, Figs. 1, 2, and 3 therein).

Figure 3 renders a typical middle-aged and fully ionised nebular structure where we see, next to the ionisation-

generated shell, already a well-developed rim. The shell is somewhat diluted because it has already expanded into the former AGB wind, while the rim is of much higher density because of the bubble's comparatively high pressure. Consequently, both the rim and the shell show a very distinct behaviour in their radial intensity distributions and their contributions to the line profiles. Note especially the rather faint signatures of the shell in [O III] in both the brightnesses and line profiles, although the shell contains most of the nebular mass, i.e. 85 % of the $0.47 M_{\odot}$ of ionised matter contained in the PN model shown in the left panel of Fig. 3. Note especially the rather low flow velocities within the rim, $\approx 12 \text{ km s}^{-1}$, as compared to the post-shock velocity of the shell, 29.5 km s^{-1} .

It is interesting to look in more detail at the different contributions from rim and shell to the total emission profiles seen in the right panels of Fig. 3. Therefore, we have decomposed numerically the total nebular line emission of this model snapshot into the contributions from rim and shell and show them, together with the relevant model structures (velocity field and ion densities) in Fig. 4. First of all, the rim contribution is similarly strong and narrow in both ions and reflects the low velocities but high densities of the rim gas. This line contribution can well be approximated by a Gaussian profile. The shell contribution is weaker but much wider because of the velocity spread within the shell: the larger this velocity spread, the wider the shell contribution in velocity space (cf. middle panel of Fig. 4).

The difference in shape between [N II] and [O III] lines is caused by the different radial density profiles of the re-

spective ions (cf. middle panel of Fig. 4). It is obvious that the shell profile resembles only poorly a Gaussian profile, but it is the only part of the total nebular emission line that allows an estimate of the true nebular expansion speed: The inflexion point at the outer flanks of the profiles (either from N^+ or O^{++}) mark closely the post-shock velocity which is, under the physical conditions found here, usually 20–25% below the shock propagation speed (see discussion in Sect. 1.4 and Corradi et al. 2007, hereafter Paper II; Jacob, Schönberner & Steffen 2013).

We note in passing that the double-shell structure seen in Fig. 3 develops from an initial configuration with a rather smooth radial density profile which falls off outwards with a gradient varying between $\alpha=2$ and 4 if one approximates the density by power-law distributions with variable α , $\rho \propto r^{-\alpha(r)}$. This smooth initial configuration reflects the assumed evolution of the mass loss along the tip of the AGB (see, for details, Steffen et al. 1998, Fig. 19 therein). This rather simple initial structure is completely reshaped firstly by ionisation and then by the stellar wind into the much more complicated configuration as seen in Fig. 3.

Given the theoretical considerations above, we conclude that the term “expansion velocity” is by no means unambiguous, even if it is based on high-resolution spectroscopy. It characterises observationally nothing else than the *spectroscopically* determined flow of matter at a certain position within an expanding shell with a radial density and velocity profile (see Fig. 3, left panel), and it is quite important for any interpretation to know whether this position is within the rim or the shell.

Likewise, the radiation-hydrodynamics simulations confirm the observations discussed in Sect. 1.1 that the velocity field even for spherical systems is by no means as simple as a $v(r) \propto r$ law. Instead, one has to consider different velocity laws for the rim and shell matter.

1.3 Kinematic ages

A quantity very often used in the literature in various contexts is the kinematic age of a PN. Its usual definition is nebular radius, taken from images, divided by a spectroscopically measured “expansion velocity”. Irrespective of the fact that one combines a (distance-dependent) quantity measured in the plane of sky with one measured along the line-of-sight, most age determinations suffer from an internal inconsistency: The nebular outer edge, i.e. that of the shell, is combined with a velocity measured for the bright rim! Additional complications are the velocity gradient within the expanding shell, the acceleration of expansion with time, and the fact that the real expansion velocity, i.e. that of the outer, leading shock, cannot be measured spectroscopically at all.

Even if one believes in a good kinematic age of the PN, the conversion of a PN’s kinematic age into a post-AGB age is, by no means, straightforward. One has to consider

- that the measured kinematic age is just the current time scale of evolution which is subject to change because of a possible accelerated expansion,
- that the nebula forms at some distance from the star at the inner edge of the receding AGB wind, and that
- there is an offset between the (assumed) zero point of post-AGB evolution and the begin of PN formation, the so-called “transition time”. The latter is quite uncertain and depends severely on the post-AGB mass-loss history and remnant mass. Different definitions exist in the literature, but a typical value may be 2000 years (cf. Fig. 2).

An insight into the correction one has to deal with for different definitions of the kinematic age gives Fig. 5. There the ratios of true model ages (= post-AGB ages) to various definitions of kinematic ages are plotted over effective temperatures of the respective central stars as predicted by our various 1D-model simulations whose principal properties are already explained above. We assume that the mass-loss history, as devised by Blöcker (1995), comes close to reality. The tracks have quite some spread caused by the different initial conditions and central-star properties, but they all show a similar run with effective temperature (or time).

We begin the discussion with the kinematic age definition $R_{\text{out}}/V_{\text{post}}$ which appears to us the best choice one can get because V_{post} characterises the flow immediately behind the shock at R_{out} which is usually also the fastest within the entire nebula (cf. Fig. 4), and because V_{post} changes only slowly with time during a significant part of the nebular expansion. However, this choice for the kinematic age leads, at least in principle for expansion with constant rate, to a systematic *overestimation* of the true age since $V_{\text{post}} \simeq \dot{R}_{\text{out}}/1.3$ (cf. Fig. 6). In reality, we have an age offset due to the finite transition time, a rapid shock acceleration during the optically-thick stage, and a low shock acceleration during the following evolution across the HRD (cf. Fig. 10 below), all of which conspire for *underestimating* the post-AGB age.

The situation is illustrated in the top panel of Fig. 5. At early stages of evolution, transition time and shock acceleration dominate and result in age underestimates by factors between 1.3 and 2.0, depending on model sequence and evolutionary stage. Later, the nearly constant expansion dominates, and the correction factors decrease slowly, but still remain above unity. Only for the $0.625 M_{\odot}$ sequence with its short transition time and the virtually constant expansion rate after the thick/thin transition, the correction factor falls below unity quite soon.

The second panel of Fig. 5 relates the model ages to rim radius divided by rim velocity, which is a consistent combination, but not used in practice. Because the rim radius is sometimes difficult to detect numerically, we used here the radius of the contact discontinuity as a proxy instead.³ Despite its internal consistency, the use of this age can not be

³ The rim is geometrically quite thin, so that $R_{\text{rim}} \simeq R_{\text{cd}}$.

recommended: The correction factors range from about 0.5 up to about 2, on the average. The reason lies in the kinematics of the rim: first the rim gas is nearly stalling, pushing the kinematic age above the models' age; later when the rim begins to accelerate (for $\gtrsim 50\,000$ K), the kinematic ages falls below the true ages.

This panel is qualitatively similar to Fig. 20 in Villaver et al. (2002), although a quantitative comparison is impossible because of the different assumptions about the zero point of the post-AGB evolution and the different definitions of “expansion” velocity and radius made in both studies.

The third panel of Fig. 5 relates the model ages to shell radius divided by rim velocity, an inconsistent method but used frequently in the literature. As expected, the result is disastrous: The mean correction factor runs from 0.2 up to close to unity for the older models. Because the rim expansion is so slow at the beginning, kinematic ages based on this method overestimate grossly the true (post-AGB) ages. Only at later stages of evolution, when the rim accelerates, the discrepancy to the true post-AGB ages decreases.

The bottom panel of Fig. 5 relates the model ages to shell radius divided by V_{av} , the mass-weighted velocity. This method, introduced by Gesicki et al. (1998), is very elaborate because it demands knowledge of (radial) density and velocity profiles of the PN. The former can be deduced from the surface brightness distribution, e.g. from H α , if spherical symmetry is imposed, but the latter has to be derived from emission lines and is not always unambiguously possible. It is mandatory that density profile and velocity field are consistent with the physics of expanding shock waves and wind-wind interaction, a constraint which is difficult to judge from observations alone. Nevertheless, neglecting the more extreme case of the “ $\alpha = 3.0$ ” sequence, a value of about 0.8 seems reasonable for typical PNe, i.e. $\text{post-AGB age} = (0.8 \pm 0.1) \times R_{out}/V_{av}$, but holding only for $\log T_{eff} \lesssim 4.9$.

It is obvious that our hydrodynamics models provide only a rather simplistic view of true nebulae. Still, the results presented in Fig. 5 suggest that measurements of flow velocities right behind the leading shock of the PN's shell is a robust and the most reliable method for estimating true post-AGB ages. But even so, errors due to asphericity, and especially the uncertainty of the transition time, make any PN age determination to a risky endeavour.

We add that the ad hoc assumption to measure a relevant expansion velocity at the 10% level of the line profile (resolved or not resolved) is, of course, also a reasonable choice if the post-shock velocity is not measurable, but one must recognise that this criterion is unphysical and does not take care of ionisation differences. This can be seen in Fig. 4 where the 10% criterion delivers a flow velocity of 33 km s^{-1} from the [N II] line, while [O III] gives 28 km s^{-1} . Only the profile's inflexion point provides the same value for both ions: 30 km s^{-1} .

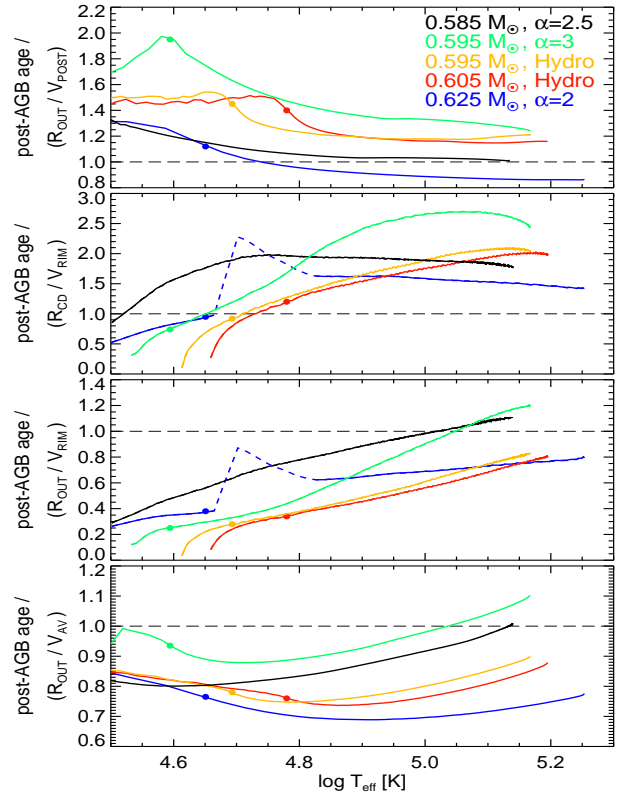


Fig. 5 Ratios of post-AGB ages to various definitions of the kinematic age as predicted from a number of hydrodynamical simulations for different post-AGB remnants and initial configurations, parameterised by stellar mass and envelope structure (slope α or “hydro”), vs. stellar effective temperatures (see, for more details, Perinotto et al. 2004; Schönberner et al. 2005a). Plotted are the age ratios only for the horizontal part of the HRD evolution until maximum stellar effective temperatures. Velocities were determined from computed line profiles broadened by a Gaussian of 6 km s^{-1} FWHM to account for the limited spectral resolution: V_{rim} from the peak separation of the strongest line components of [O III], and V_{post} from the (outer) inflexion points. Dots along the sequences indicate the position of the optically thick/thin transition if not below $\log T_{eff} = 4.5$. The color coding of the tracks will remain the same throughout the paper. The dashed part of the 0.625 M_{\odot} track seen in the two middle panels will be explained later (Sect. 4.2). Note also the different ranges of the ordinates. *Top panel*: kinematic age defined as (outer) shell radius, R_{out} , over post-shock velocity V_{post} . *Second panel*: kinematic age defined as radius of contact discontinuity, R_{cd} (as proxy of R_{rim}), over velocity of the rim, V_{rim} . *Third panel*: kinematic age defined as shell radius, R_{out} over V_{rim} . *Bottom panel*: kinematic age defined as shell radius, R_{out} , over mass-averaged velocity, V_{av} .

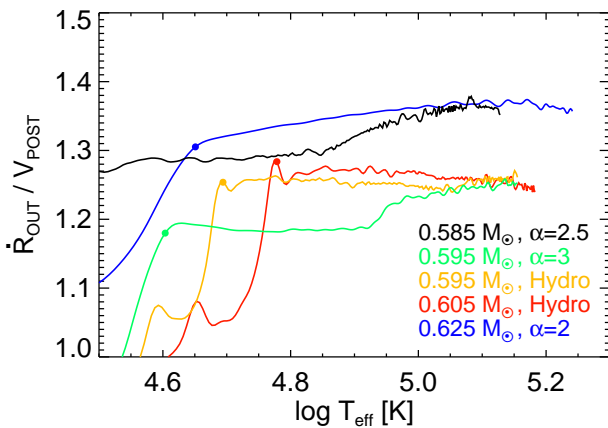


Fig. 6 Ratio of outer shock velocity, \dot{R}_{out} , and post-shock velocity, V_{post} , vs. stellar effective temperature as predicted by hydrodynamical sequences with different initial conditions and central stars with various masses (see legend). Only the results for the high-luminosity part of evolution through the HRD until maximum stellar temperatures are reached are shown. The rapid increase of $\dot{R}_{\text{out}}/V_{\text{post}}$ from about unity to 1.2–1.3 belongs to the optically thick part of evolution whose end is marked by a dot.

1.4 The relation between shock and post-shock velocity

The post-shock velocity, i.e. the flow velocity immediately behind the shell’s leading shock (or the shell’s outer edge), is a well-defined physical quantity and is related to the shock’s propagation speed via the well-known jump conditions. For instance, the relation between both velocities depends on the shock properties (adiabatic, isothermal, or intermediate) which are ruled by the physical state of the flow and the environment into which the shock expands. A thorough discussion for the specific case of planetary nebulae has been presented in Mellema (2004) and Schönberner et al. (2005b).

Figure 6 shows how the relation between shock and post-shock velocities, as predicted by our hydrodynamical PN simulations, depend on evolutionary state (again measured by the stellar effective temperature) and model parameters. One sees that the ratio of both velocities does not vary much between the different model sequences: typical values for optically-thin models are between 1.2 and 1.35, with very little variation during the evolution across the HRD. The only exceptions are the transition phases from optically-thick to an optically-thin model where the velocity ratio “jumps up”.

The ratios of shock to post-shock velocity shown in Fig. 6 agree very well with the value estimated by Mellema (2004). Based on the analytical solutions of Chevalier (1997) and Shu et al. (2002), he concluded that this ratio is, for the case of typical PN conditions, around 1.20.

The close correspondence between the propagation speed of the shell’s shock and the post-shock velocity seen

in Fig. 6 allows us in the following to use the post-shock velocity as a proxy for the nebular expansion: All expansion properties found from spectroscopic determinations hold also for the outer shock, apart from a scaling factor of about 1.3.

1.5 A modern observational approach

From the previous sections it becomes evident that a more thorough discussion of the general problem of the expansion of PNe is urgently needed, as well as a physically sound interpretation of the observed line profiles. This implies the necessity to observe line profiles with high signal-to-noise in order to get hold of weak outer signatures of fast moving gas immediately behind the leading shock front combined with radiation-hydrodynamics simulations for a proper interpretation. Knowing the true expansion behaviour of PNe is mandatory for estimating total lifetimes of PNe or mean visibility times belonging to PN ensembles in stellar populations (cf. Jacob, Schönberner & Steffen 2013).

A first study to gain closer insight into the expansion behaviour of planetary nebulae, especially in terms of the different properties of shell and rim, has already been presented by Schönberner et al. (2005b). Basically, these authors determined typical bulk velocities of the rim and the shell matter by means of Doppler decomposition of strong emission lines gained by high-resolution spectroscopic observations into four Gaussians and compared them with theoretical line profiles computed from appropriate radiation-hydrodynamics simulations. The theoretical profiles were decomposed into four Gaussians in exactly the same way as the observed ones.

Schönberner et al. (2005b) found a significant increase of typical bulk velocities of rim and shell with progress of evolution, the latter measured by the effective temperature of the central star. The expansion of the shell turned out to be very fast, up to about 30–40 km s^{−1}. Schönberner et al. were then able to interpret this expansion by means of radiation-hydrodynamics simulations: A PN expands into a circumstellar environment whose radial slope is much steeper than usually assumed, $\rho \propto r^{-\alpha}$ with $\alpha > 2$. This result is fully consistent with the very few existing direct measurements of the radial density profiles of halos from their surface brightness distribution (Plait & Soker 1990; Corradi et al. 2003; Sandin et al. 2008).

The PNe sample investigated by Schönberner et al. (2005b), however, was rather small, and additional data from the literature was not available at the time. Since a detailed velocity information of a much larger sample of round/elliptical PNe appears to be necessary to strengthen the conclusions mentioned above, the Schönberner et al. sample was increased by new high-resolution spectroscopic observations with very good signal-to-noise ratios. Only if the sample is sufficiently large, a meaningful comparison with (spherical) hydrodynamical models can be made which then will give important constraints on the physical condi-

tions responsible for the formation and evolution of planetary nebulae.

In the present work we took up the method recommended in Paper II. There, we showed that the derivative of the line profile allows an rather accurate determination of the post-shock gas velocity of the shell. Knowing the post-shock velocity, the conversion to the true expansion velocity, i.e. the propagation velocity of the outer shock, is simple (see discussion in Sect. 1.4). This is the optimum one can get since, as already said, the propagation speed of the shock itself cannot be measured spectroscopically.

In Sect. 2 we report on our observations, the profile extraction and the determination of the respective expansion velocities which are then presented in Sect. 3. Section 4 is devoted to detailed comparisons with predictions of radiation-hydrodynamics simulations. In Sect. 5 we present, for the first time, apparent expansion asymmetries along the line-of-sight seen in some objects. Next, in Sect. 6, the expansion behaviour of very evolved PNe harbouring hot white dwarfs as central stars is discussed. Section 7 deals then with the expansion of metal-poor objects. A discussion of the results follows in Sect. 8, and the conclusions (Sect. 9) close the paper. – We note that preliminary results of this study have been published in Jacob et al. (2012).

2 Observations and data reduction

2.1 Planetary nebulae in the Galactic disk

We selected our targets from a list of Galactic disk PNe with well developed double-shell structures which do not deviate too much from a spherical shape. We verified that the central stars are not belonging the Wolf-Rayet spectral class since the evolution of these hydrogen-poor objects is still poorly understood and certainly not adequately described by the evolutionary calculations available.

We observed our sample in 1999 July and 2000 January with the Coudé-échelle spectrograph attached to the 2-m telescope in Tautenburg, Germany. The (projected) slit length was $29''$ with a width of $0''.9$, providing a resolving power of $\lambda/\Delta\lambda = 48\,700$, corresponding to 6 km s^{-1} . The slit was positioned such that it contained the central star in order to get the full velocity separation for rim and shell. The slit width was always very small compared to the object sizes. The useful spectral ranges were $4700\text{--}5800\text{ \AA}$ and $5490\text{--}6760\text{ \AA}$, respectively. The detector used was a $15\text{ }\mu\text{m}$ SITE-CCD, giving a spatial resolution of $0''.5\text{ pix}^{-1}$. The typical seeing during the observations was between $2''$ and $3''$. We tried to chose the exposure times such that also the fainter shoulders of the emission lines have sufficient signal. Most objects were observed at least twice.

The spectra were reduced and calibrated using standard ESO-MIDAS packages. Spectrum reduction included bias and straylight subtraction, filtering of cosmic ray events, flat fielding, order extraction, and wavelength calibration using a ThAr lamp. In the result, we obtained one 2D-image for

each échelle order. From these, we extracted the profiles of the strong [N II] and [O III] lines, and those of $H\alpha$ as well, using the central pixel row along the cross-dispersion direction. Where necessary, the spectra of the adjacent rows on either side were also extracted and co-added in order to improve on the S/N.⁴

Most of our targets are still in the stellar high-luminosity phase of their evolution, and examples of the line profiles are displayed in Fig. A1 of the Appendix, altogether for 15 PNe. Few objects are in a later phase of evolution where recombination of the outer nebula parts had already occurred and which appear now to be in the reionisation stage. Analysis and discussion of these objects are postponed to Sect. 6.

The appearances of the line profiles are very similar and reflect the similarity of the apparent morphologies. The two main line components of the receding and approaching parts of the nebular shell are usually split into two subcomponents with separation and relative strength that reflect the kinematical state of the respective object: The inner of these subcomponents, which is the signature of the bright rim, are usually flanked by much fainter shoulders (more pronounced in the light of [N II]) whose positions indicate velocities much higher (up to about seven times, see Fig. 12) than those typical of the bright rim. The line emission of these shoulders originating from the shell is sometimes very weak and can easily escape detection in spectrograms of insufficient S/N, although they are, as we have seen, of utmost importance for interpreting expansion properties of PNe. It is obvious that any detailed information on nebular kinematics is *not* retrievable from hydrogen (or helium) lines because of their high thermal broadening (cf. $H\alpha$ profiles shown in Fig. A1).

We retrieved the kinematical informations from the line profiles in the following way: Firstly, we decomposed the whole line profile into four Gaussians and identified the two innermost, strongest components to be representative for the flow of the gas belonging to the rim. Then we used the line profile derivatives to determine the (outer) inflexion points of the shoulder profiles, i.e. we determined the outermost extremes of the derivatives. It was demonstrated in Paper II that, based on radiation-hydrodynamics models, these reflexion points correspond very closely ($\pm 1\text{ km s}^{-1}$) to the post-shock velocity of the shells (see also Fig. 4). The method is illustrated in detail in Fig. 7 for NGC 6826.

We note that this method demands an extremely high quality of the observations, which was not always met. In these cases where the derivative could not be used we took the two additional Gaussians as substitutes of the shell emissions and used their (outer) inflexion points as representative of the post-shock velocity. We verified by means of high-quality line profiles that the positions of the shell inflexion points from the line profile agree reasonably well

⁴ We did not make use of the velocity ellipses because the extent of many targets were not fully covered by the slit. The stellar continuum is much too faint as to disturb the strong emission lines, especially for the high spectral resolution used here.

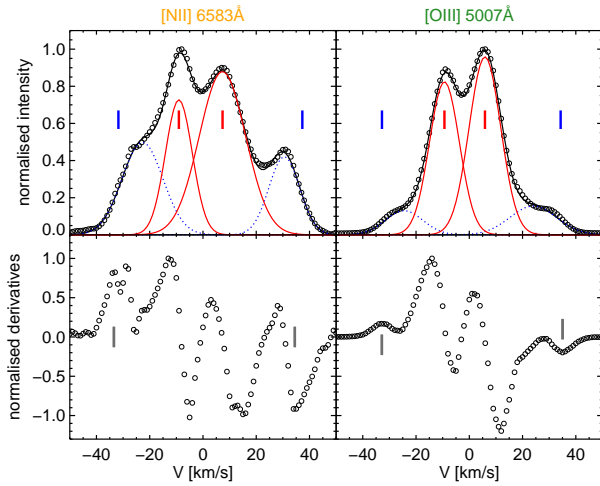


Fig. 7 Examples of high-resolution, high signal-to-noise line profiles (open symbols) and their decompositions into 4 Gaussians (blue dotted and red solid) (*top*) and line profile derivatives (*bottom*) from [N II] (*left*) and [O III] (*right*) for the PN NGC 6826, from spectrograms taken at Tautenburg observatory. The sum of the four Gaussians is shown in black solid (*top*). Vertical dashes in the *top* panels mark either the positions of the two rim components (as follows from the decomposition), or the outer inflection points of the shell Gaussians (center of Gaussian \pm sigma). The dashes in the *bottom* panels indicate the outer inflexion points of the observed line profile (corresponding to the outer relative extremes of the derivatives).

with those derived from the Gaussians. In the example shown in Fig. 7 there exists for [N II] only a small difference between both methods, $\Delta V \lesssim 2 \text{ km s}^{-1}$.

In passing we note the obvious asymmetry seen in the line profiles of NGC 6826 as shown in Fig. 7: (i) The velocity difference between rim and shell is higher for the receding part of the nebula compared to the approaching part, and (ii) this velocity asymmetry seems to be correlated with a difference in the strength of the two rim components, most notably in the [N II] profile. We will discuss this issue in more detail in Sect. 5.

All individual velocities measured by profile decompositions and derivatives are collected in Table A1, with references to previous works. The typical error for an individual velocity measurement is $\pm 1 \text{ km s}^{-1}$ for velocities of the rim components (peak separation of the Gaussian fits) and $\pm 2 \text{ km s}^{-1}$ for the post-shock velocities of shells (separation of the derivative extremes). Systematic errors due to slit position and poor seeing can be larger, i.e. up to $\pm 3 \text{ km s}^{-1}$.

All velocities for a line component and ion listed in Table A1 were (if possible) averaged over the individual measurements and compiled in Table 1, together with the respective central-star temperatures taken from the literature. We supplemented the Tautenburg sample by objects from the work of Schönberner et al. (2005b, Table 4 therein). These additional objects were observed either at La Silla

Table 1 Mean values of measured rim and shell (post-shock) velocities, deduced from the profiles of [O III] 4959/5007 Å and [N II] 6548/6583 Å, and effective temperatures of the central stars for Galactic disk objects. The velocity data are from Table A1 (Tautenburg), supplemented by reanalysed data from observations taken at ESO or La Palma (Schönberner et al. 2005b).

Object	$V_{\text{rim}} \text{ (km s}^{-1}\text{)}$		$V_{\text{post}} \text{ (km s}^{-1}\text{)}$		$\log(T_{\text{eff}}/\text{K})$
	[O III]	[N II]	[O III]	[N II]	
Tautenburg:					
IC 289	25	–	47	–	5.00 ²
IC 3568	9	9	33	31	4.70 ¹
IC 4593	3	4	22	24	4.60 ¹
M2-2	11	11	36	–	4.90 ⁵
NGC 2022	29	–	–	–	5.00 ²
NGC 2610	33	–	–	–	5.00 ²
NGC 3242	16	18	39	40	4.87 ¹
NGC 6543	16	21	–	45	4.82 ⁶
NGC 6826	8	9	32	34	4.70 ¹
NGC 6884	–	19	–	–	4.94 ³
NGC 6891	7	7	32	34	4.70 ¹
NGC 7009	18	18	36	–	4.91 ¹
NGC 7354	24	27	44	44	5.00 ³
NGC 7662	26	27	–	–	5.00 ³
Vy 2-3	9	–	35	–	4.78 ³
ESO or La Palma:					
IC 418 *	< 5	–	–	13	4.56 ¹
IC 2448 *	18	18	35	–	4.81 ¹
M1-46	–	12	–	32	4.65 ⁴
My 60 *	23	24	38	–	5.02 ³
NGC 1535 *	22	–	32	–	4.85 ¹
NGC 2610 *	34	–	42	–	5.00 ²
NGC 5882	–	22	–	47	4.83 ³
NGC 6629	–	6	–	34	4.67 ¹
NGC 7662 *	26	–	35	–	5.00 ³
Tc 1	–	12	–	30	4.52 ¹

Notes: * V_{post} from long-slit spectrograms (Paper II). Stellar temperatures are from: ¹ Méndez, Kudritzki & Herrero (1992), ² McCarthy, Méndez & Kudritzki (1997), ³ He II Zanstra temperature (Gorny, priv. comm.), ⁴ Guerrero et al. (1996), ⁵ Aller & Keyes (1987), ⁶ Georgiev et al. (2008).

(ESO/CAT or NTT) or on La Palma (NOT), and the line profiles were reanalysed in the same way as described here. For some objects (annotated in the table), V_{post} was taken from the analyses of long-slit spectrograms reported in Paper II.

2.2 Planetary nebulae in the Galactic halo

The mean nebular oxygen abundance of the objects of our sample listed in Table 1 is, according to Henry et al. (2004), $\langle 12 + \log(\text{O}/\text{H}) \rangle = 8.65$, with a 1σ dispersion of 0.10 dex only.⁵ This average oxygen abundance can be considered

⁵ More precisely, this mean abundance is based on 14 objects out of the 27 listed in Table 1 which are in common with the compilation of Henry

as typical for Galactic disk PNe. Since oxygen is the main cooling agent in a PN, we use it here as a convenient proxy for the overall metallicity Z .

The rather small variation of the oxygen abundance within our PN sample in Table 1 renders any study of the dependence of the expansion velocity (i.e. of V_{post}) on metallicity impossible. A better control sample is certainly provided by metal-poor nebulae, such as found in the Galactic halo. We selected four targets from the list of metal-poor (halo) PNe provided by Howard et al. (1997), BoBn 1, M2-29, PRMG 1, and Ps 1, the nebula around K648 in M 15.

These four metal-poor PNe were observed in August 2006 by C. Sandin at the VLT with the FLAMES/ARGUS integral-field unit (Program 077.D-0652, PI D. Schönberner). Two spectral regions were observed, 4911–5158 Å (HR8) and 6383–6626 Å (HR14B), with resolutions of 32 000 and 46 000, resp. The seeing was below 1'', sufficiently good to ensure full spatial resolution of the targets. The reduction of the data was performed using the standard Giraffe reduction pipeline 2.5.3, and from the resulting 2D spectra the (final) 1D spectrum for the central line-of-sight was retrieved for further analysis. The presentation of relevant line profiles and their detailed interpretation in terms of expansion velocities is postponed to Sect. 7.

3 General expansion properties

3.1 Rim and shell velocities of high-luminosity PNe

A comparison with results from the literature, notably from the catalogue of Weinberger (1989), is not straightforward since no reference to faint outer wings is given, and also the details of the measurements and the errors are difficult to judge. Assuming that the listed velocities refer to the peak separation of the line profiles, there exists fair agreement with our rim velocities (cf. Table A1). Only in rare cases more recent measurements of much higher velocities, comparable to our post-shock results, are available.

For three objects (NGC 2022, NGC 3242, and NGC 7662) a comparison of the results from the Tautenburg spectrograms with the previous measurements by Schönberner et al. (2005b), which are also based on high-resolution spectra and treated in the same way, was possible. The agreement is excellent, with deviations of less than 2 km s^{-1} (rim only).

More interesting is the internal consistency between results from [N II] and [O III]. This is illustrated in Fig. 8 for those objects where both velocities are available (cf. Table 1). A close 1:1 relation between the velocities from [N II] and [O III] lines is to be expected for optically thin nebulae since both ions extend over the whole PN, although with different abundances. This is indeed the case for the post-shock velocity: Within the errors, the values

et al. (2004). The more recent determinations by Pottasch & Bernard-Salas (2010) yield $\langle 12 + \log(\text{O}/\text{H}) \rangle = 8.54$, also with a 1σ dispersion of 0.1 dex, but from 7 common objects only.

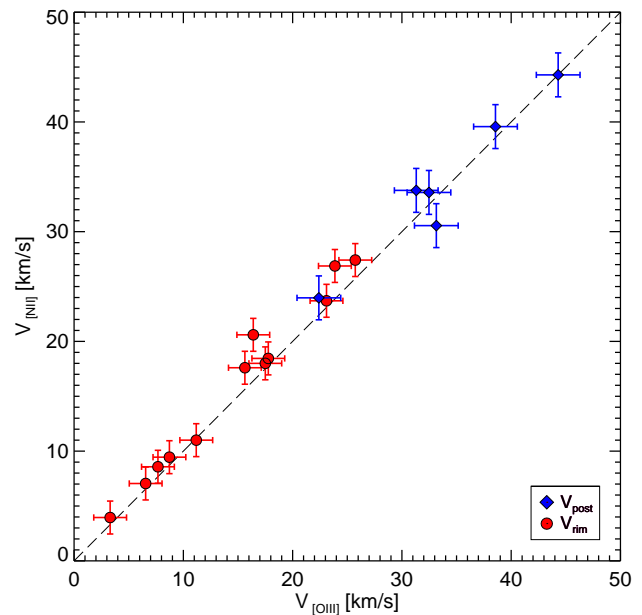


Fig. 8 Comparison of measured rim velocities (red dots) and shell post-shock velocities (blue diamonds) based on [N II] and [O III] lines as listed in Table 1 for those objects for which values from both ions are available, with appropriate error bars. The dashed diagonal line is the 1:1 relation. Note also that not for all rim entries a corresponding shell post-shock value does exist.

from [N II] and [O III] do agree. The same holds for V_{rim} of young objects with low rim velocities.

There appears, however, a small offset between velocities from [N II] and [O III] at higher rim velocities in the sense that the [N II] values are higher by a few km s^{-1} . This indicates the development of a positive velocity gradient within the rim during the PN evolution (cf. Wilson 1950). However, in the following discussion we neglect these small differences and use averages if both velocities are available.

Notes on individual objects For five objects (IC 289, IC 3568, IC 4593, NGC 6543, and NGC 7009) we detected the signatures of the attached shells in the central line profiles for the first time and measured the corresponding post-shock velocities. In four cases (NGC 2022, NGC 2610, NGC 6884, and NGC 7662) we were unable to detect/measure the faint shell emission in the central line profile. Attached shells are well-known from the images, but their signatures in the line profiles are masked because of too small velocity differences between rim and shell. In these cases post-shock velocities can only be determined by means of long-slit spectrograms (see Paper II and NGC 2610 and NGC 7662 in Table 1).

NGC 2022 belongs morphologically also to the class of nearly round double-shell PNe, yet it is an exception because its shell edge obviously expands slower than the rim, as is evident from the long-slit spectrograms taken by Sab-

badin et al. (1984). We estimate a post-shock velocity of about 20 km s^{-1} from their position-velocity diagrams.

IC 418 from the La Palma sample is a very young, compact PN with a cool central star ($\simeq 36000 \text{ K}$) which is just at the verge of becoming optically thin (Morisset & Georgiev 2009; Ramos-Larios et al. 2012). For this very reason, our method for the determination of the post-shock velocity is not going to work since the regular double-shell structure is not yet existent. Instead, we proceeded as follows: We know from our simulations that this particular phase is characterised by a maximum of the shock velocity (cf. Schönberner et al. 2005a, Fig. 4, left panels). From the models we estimated a correction of 5–10% necessary for converting the velocity from the $[\text{N II}]$ peak separation (12.5 km s^{-1} , Schönberner et al. 2005b) into the post-shock velocity, i.e. $V_{\text{post}} = 13.5 \text{ km s}^{-1}$. The shock velocity itself is then $13.5 \times 1.25 = 17 \text{ km s}^{-1}$.

3.2 Kinematics and evolution

The total combined sample of double-shell PNe with accurate velocity information for both the rim (bulk gas velocity) and shell (post-shock velocity) spans, as one can judge from the stellar temperatures, a wide range of evolutionary stages and is about twice as large as the sample used by Schönberner et al. (2005b). For the following interpretations we prefer here again, as in Schönberner et al. (2005b), the use of the effective temperature of the central stars as a distance-independent proxy for the evolution in time.⁶

Figure 9 is an improvement of Fig. 12 (top) in Schönberner et al. (2005b) and presents a general velocity evolution of rim and shell while the star crosses the HRD. A qualitatively similar diagram (many objects in common with our sample) can be found in Méndez et al. (1988, Fig. 5b therein), but it gives the velocity from the half-width of $\text{H}\gamma$ only, i.e. without any discrimination between rim and shell velocities. Nevertheless, the basic trend is the same as here: The velocities increase with stellar temperature. The main results from Fig. 9 are the following:

- The shell’s edge expands considerably faster than the rim, but both accelerate during the evolution, albeit in a different way. The post-shock velocity of the shell increases with T_{eff} from about 25 km s^{-1} up to about 40 km s^{-1} at $\log T_{\text{eff}} \gtrsim 4.8$. In contrast, the rim is stalling at rather low velocities ($\simeq 5\text{--}10 \text{ km s}^{-1}$) for quite a while until it accelerates up to about 30 km s^{-1} .

Because of this different evolutionary behaviour, the velocity difference between rim and shell changes from initially $\sim 20\text{--}25 \text{ km s}^{-1}$ to about 15 km s^{-1} only, making it more difficult to detect the shell signature in the

⁶ The use of the stellar temperature is of advantage because both the radiation field and the wind power of a central star are directly related to its effective temperature during the horizontal part of evolution across the HR diagram, and both are also the main drivers of PN evolution. A second advantage is that the total effective temperature range varies only rather modest with central star mass, which means that the effective temperature is not closely related to age, unless all central stars have the same mass.

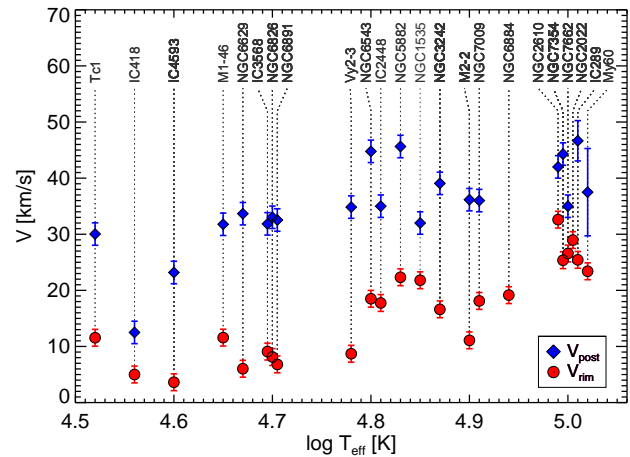


Fig. 9 Shell post-shock velocities, V_{post} (blue diamonds) and rim velocities, V_{rim} (half of line peak separation, red dots) of the objects listed in Table 1 vs. the effective temperatures of the respective central stars. There are generally two velocity entries for each object, except for those for which the post-shock velocity could not be measured (NGC 2022 and NGC 6894). Velocities are either from $[\text{N II}]$ or $[\text{O III}]$, or averaged if information from both ions is available (cf. Table 1). Vertical dotted lines connect the two velocities with the object’s name. Some object entries are slightly shifted in temperature as to avoid overlapping.

line profiles of evolved objects (cf. notes on individual objects).

- The initial shell expansion starts with post-shock flow speeds *higher* than the typical AGB outflow velocities of $\approx 10\text{--}15 \text{ km s}^{-1}$.⁷ The rim gas, however, has initial velocities which are roughly equal or even well below the typical AGB outflow velocities. Typically for these young PNe is that the post-shock velocity of the shell exceeds the rim expansion by factors up to more than six ($\simeq 3.5 \text{ km s}^{-1}$ vs. $\simeq 23 \text{ km s}^{-1}$ for IC 4593)!

Our results are consistent with those in Fig. 12 of Schönberner et al. (2005b), and the interpretation of Fig. 9 is then the following: At first, as the AGB remnant heats up, photoionisation is at work and forms an ionised shell out of the neutral AGB matter which is still slowly expanding with about $V_{\text{agb}} \simeq 10\text{--}15 \text{ km s}^{-1}$. The leading edge of this shell – the D-type shock ahead of the ionisation front – accelerates into the AGB wind and attains velocities well above V_{agb} . At the same time, the inner part of the shell becomes decelerated because the thermal pressure of the wind-blown bubble falls short of the increasing shell pressure. The reason is the initially rather low wind speed (or wind luminosity) (see, e.g., Fig. 2, right panels). Nevertheless, a (proto-) rim forms slowly as the stellar wind gains power with time (cf. left panel in Fig. 3), but its outward velocity remains rather low for quite a while.

⁷ The real expansion velocity of the shell is given by the shock propagation which is even higher than the post-shock velocity (see Sect. 4).

As evolution across the HRD progresses, the nebula becomes optically thin, which means that the ionisation front overtakes the shock and enters the so-called “champagne phase” of expansion (Tenorio-Tagle 1979; Chevalier 1997). Since the wind power of the central star, $L_{\text{wind}} = \dot{M}V_{\text{wind}}^2/2$, increases steadily (cf. Fig. 2, middle panel), and because a certain part of the kinetic wind energy is converted into thermal energy of the hot bubble, the rim is being accelerated into the shell, thereby sweeping up shell matter. This is the double-shell phase during the evolution of a PN, depicted also in Fig. 3.

4 Comparisons with radiation-hydrodynamics simulations

Before continuing with this section, we emphasise that none of our 1D-radiation-hydrodynamics simulations presented in this work are aimed at fitting any particular object. They are too simple with respect to geometry, and they are thus only used in helping to interpret our observations. But we believe that, due to the very detailed physics implemented, our models give, on the average, a realistic description of the most important aspects of real PN evolution.

4.1 The shells

Figure 10 is again an extended and modified version of Fig. 12 (bottom) of Schönberner et al. (2005b), displaying now the post-shock velocities for our sample of PNe from Table 1 together with the predictions of (optically thin) hydrodynamical models with simplified initial conditions as explained in Schönberner et al.. In short, all model nebulae have the same central star of $0.595 M_{\odot}$ and expand into an environment whose density falls off according to a power law, $\rho \propto r^{-\alpha}$, with constant α (the only exception is the “hydro” sequence where α increases with distance from the star).

Figure 10 (top panel) illustrates convincingly how strong the velocity behind the leading shock depends on the radial density slope of the upstream matter. The modest acceleration is due to the electron temperature increase while the star heats up (cf. Figs. 3 and 5 in Schönberner et al. 2005b) and to a slight steepening of the density gradient with time (see below). The initial AGB wind velocity must be considered, too, because theory predicts shock (and post-shock) velocities *relative* to the upstream flow. An $\alpha = 3$ model sequence with higher AGB-wind speed (20 km s^{-1}) is plotted in Fig. 10 (top panel) for comparison. The range of AGB wind velocities observed is, however, only a few km s^{-1} ($\lesssim 5 \text{ km s}^{-1}$) to either side of a typical value (10 km s^{-1} is assumed here). Correspondingly, part of the observed velocity spread may result from different AGB velocities.

The interpretation of Fig. 10 (top panel) is then the following: Most objects expand like the “ $\alpha = 3$ ” model, but

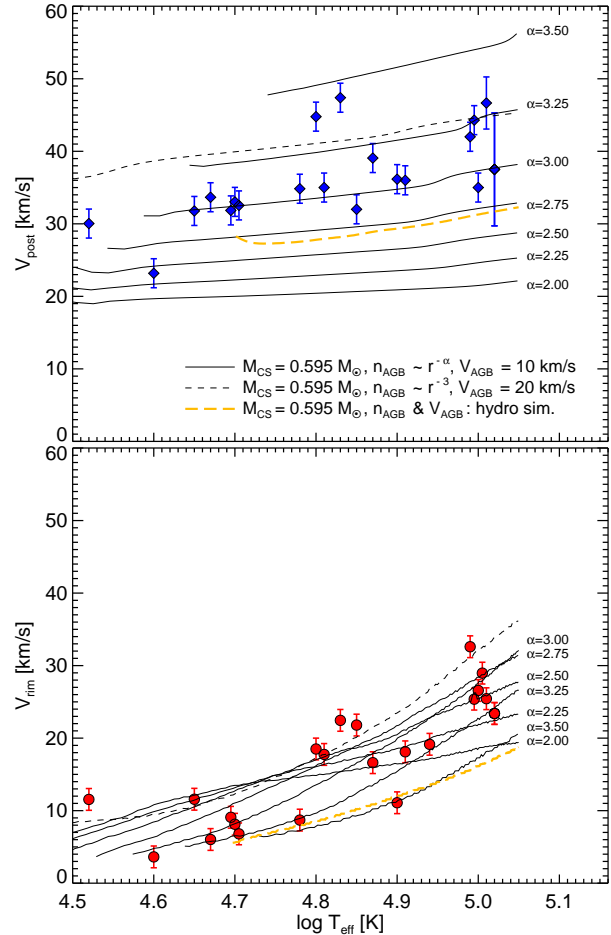


Fig. 10 Observed post-shock velocities (*top*) and rim velocities (*bottom*), both from Fig. 9, compared with predictions from a series of model simulations with the same central-star model, as indicated in the figure legends. Only the optically thin models are plotted (consequently, IC 418 is omitted). In both panels, the thin lines belong to models that expand into ambient matter with power-law density profiles, characterised by the initial exponent α . The original AGB-wind velocity is 10 km s^{-1} (solid) or 20 km s^{-1} (short dashed), for $\alpha = 3$ only in the latter case. The long-dashed lines belong to a “hydro” model. For more details, see text.

some have steeper density gradients, one (IC 4593) obviously a flatter upstream density profile. We note that our “hydro” model expand a bit too slowly (cf. long-dashed line in Fig. 10): The reason is the still rather modest (initial) density gradient which is comparable to an $\alpha \simeq 2.7$ model for that part of the evolution that is shown in the figure.

Direct density profile determinations of halo matter have been performed by Plait & Soker (1990) and, more recently, by Sandin et al. (2008). Both groups converted the halo surface-brightness profiles of a few objects (IC 3568, M2-2, NGC 6826, NGC 7662) into density profiles by means of an Abel transformation. Plait & Soker (1990) found $\alpha' = 4$ for the halo of NGC 6826, whereas Sandin et al. (2008) deter-

mined the following average values: $\alpha' = 5.6$ (IC 3568), 4.5 (M2-2), 4.2 (NGC 6826), and 4.6 (NGC 7662).⁸

Using the images presented in Corradi et al. (2003), we were able to measure the surface brightness gradient of the halo in front of the leading shell edge for six objects from Table 1: IC 2448, NGC 1535, NGC 2022, NGC 3242, NGC 6826, NGC 7009, and NGC 7662. We adopted an inner and outer radius for the gradient determination at roughly 1.1 and 1.3 shell radii. The slope was then measured at 36 position angles in the haloes, and averaging the results for H α + [N II] and [O III] where both are available (there are no significant differences between the H α and [O III] measurements). Excluding NGC 2022 (see below), the average surface brightness slope is characterised by $\gamma = 5.2 \pm 0.2$, with $SB \propto p^{-\gamma}$, where p is the impact parameter. Individual values range between 5.0 and 5.5, with corresponding errors between 0.1 and 0.7. The main sources of these errors are brightness irregularities and small deviations from sphericity.

For converting the average halo intensity slope γ into a corresponding density slope α' we used the approximation $\alpha' = (\gamma + 1)/2$ and got $\alpha' = 3.1 \pm 0.1$ for the average upstream halo density slope of the five PNe listed above (NGC 2022 excluded).⁹ We tested this approximation by using our radiation-hydrodynamic models and proceeded in the same way as for the real objects. We found a very good consistency between γ and α' for $\alpha = 2$ models, but for $\alpha > 2$ the above approximation tends to underestimate the density slope. For instance, our $\alpha = 3$ models suggest that the present density slope is underestimated by about 0.3. Keeping this in mind, we estimate an average value of $\alpha' \simeq 3.4$, i.e. a bit higher than the mean initial value $\alpha \simeq 3.1$ read off from Fig. 10 (top panel). The five considered PNe have, on the average, a post-shock velocity of 35 km s^{-1} , with a 1σ dispersion of 3 km s^{-1} .

The direct comparison of our measurements with those of Sandin et al. (2008) is possible only for two objects, NGC 6826 and NGC 7662. Our individual values for α' , 3.3 ± 0.2 and 3.2 ± 0.3 , fall short of Sandin et al.'s values 4.2 and 4.6, resp., even if one corrects our values by $+0.3$. One must keep in mind, however, that both methods trace different halo regimes: The Abel transformation used by Sandin et al. (2008) considers the entire but finite halo brightness distribution and corrects implicitly also for possible projection effects, under the assumption of strictly spherical symmetry. Our method traces only the halo region immediately ahead of the shell and averages over possible asymmetries. Also, the role of straylight from the bright nebula must be investi-

gated and possibly considered. Given all these uncertainties and the individual errors, we believe that both methods give fairly consistent results.

A separate discussion is needed for NGC 2022 whose post-shock velocity is, quite unusually, lower than V_{rim} ($\simeq 20 \text{ km s}^{-1}$ vs. 29 km s^{-1} ; see Table 1 and notes at end of Sect. 3.1). We measured a halo surface-brightness slope of $\gamma = 2.7 \pm 0.6$, resulting in a density slope $\alpha' = 1.9 \pm 0.3$ only! Our $\alpha = 2.0$ model displayed in Fig. 10 (top panel) expands, without virtually any acceleration, with a post-shock velocity of $\simeq 20 \text{ km s}^{-1}$, in excellent agreement. Note that the rim of NGC 2022 expands with 29 km s^{-1} as is typical for objects with hot central stars (cf. Table 1 and bottom panel of Fig. 10).

The determination of halo density profiles and their comparison with the respective expansion (= post-shock) velocities provide a direct observational proof that the nebular expansion is ruled by the upstream density profile, as radiation-hydrodynamics predicts. The implication of the observed high expansion rates (V_{post} up to $\approx 40 \text{ km s}^{-1}$) is that the shells expand into halos whose initial density profiles can be characterised by a power-law $\rho \propto r^{-\alpha}$ with $\alpha \approx 3$. Assuming constant outflow velocities, AGB mass-loss rates must steadily increase until they stop suddenly at the very end of AGB evolution when the remnant is already rapidly evolving off the AGB. More details can be found in Sandin et al. (2008). Exceptions like NGC 2022 seem to be quite rare.

The hydrodynamical simulations along the final AGB evolution performed by Steffen et al. (1998) suggest that the mass-loss increase is large when the star recovers from the luminosity dip after a thermal pulse (cf. their Fig. 2). In contrast, immediately before the following pulse, luminosity, and hence mass-loss rate, remains nearly constant. If a star evolves off the AGB shortly before the next pulse, the density slope of the AGB wind envelope should be close to an $\alpha = 2$ case. One is then tempted to assume that NGC 2022 is in such a thermal-pulse cycle phase, implying that it is a candidate for a late or very late thermal pulse, i.e. for a thermal pulse occurring during its way to become a white dwarf, like, e.g., the case of FG Sge. The normal case would then be that stars leave the AGB well before the next thermal pulse and develop AGB envelopes with steep density gradients.

4.2 The rims

The rim is thought to be an example of a wind-compressed shell of matter whose expansion is controlled by the (thermal) pressure of the shock-heated stellar wind matter (i.e. the hot bubble) from within and the density and velocity of the shell matter immediately ahead of the rim's shock (cf. Koo & McKee 1992). Hence, with given properties of the ambient medium, only the evolution of the stellar mechanical luminosity (or wind power) is relevant for the kinematics of the rim gas.

⁸ We used α' (instead of α) to characterise the actual halo density gradient because the upstream density slope steepens continuously with time once the PN becomes optically thin and the halo heated by photoionisation. For instance, starting with a power law exponent of $\alpha = 3.0$, one ends up with an (upstream) exponent $\alpha' = 3.7$ once the stellar temperature has passed 10^5 K ! This effect is the higher the steeper the initial density slope.

⁹ We assume an infinitely extended halo with density slope $\rho \propto r^{-\alpha'}$ and approximate its surface brightness/intensity in an emission line at impact parameter p , $SB \propto p^{-\gamma}$, to be proportional to $(1/p^{\alpha'})^2 p$.

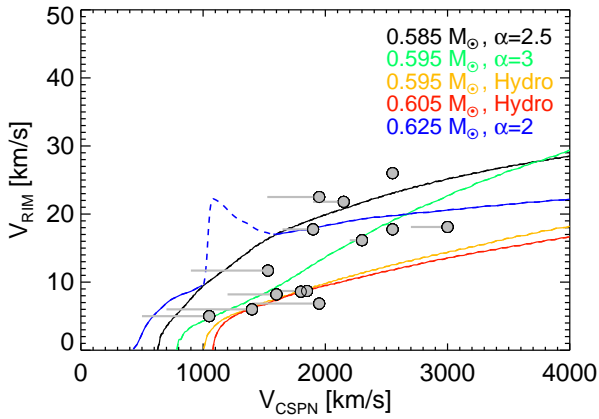


Fig. 11 Rim matter expansion, V_{rim} , of objects from Fig. 9 for which also wind velocities, V_{wind} , of their central stars are available from the literature (cf. text). The length of the horizontal bars indicates the range of stellar wind velocities reported in the literature, and the object symbols are placed at the high-velocity end of the respective bars. The curves give the corresponding model predictions for various sequences as listed in the legend. The theoretical profiles are broadened by a Gaussian with 6 km s^{-1} FWHM, and V_{rim} is determined from the peak separation of the strongest line components. The dashed part of the $0.625 M_{\odot}$ simulations indicates a transient phase in which the shell component gets stronger than the rim component, i.e. the rim velocity could not be properly traced.

The bottom panel of Fig. 10 compares our measured rim velocities with the model predictions. Generally, the rim evolution is determined by the accumulated rim mass and the shell's expansion property: Low- α sequences start with low rim masses, hence with higher speeds, but later the rim does not accelerate much because of the rather slow shell expansion. For high- α sequences, the situation is opposite: The rim starts slowly, but accelerates later. In any case, the models cover the observed range of rim velocities and their evolution with stellar temperature. The rim velocities of our “hydro” sequence constitute the lower bound of the observations.

Whereas central-star mass-loss rates are only rather poorly known quantities, the wind velocities are much better observationally constrained. Also, from the theory of radiation-driven winds follows that mass-loss rates do not change very much during the evolution across the HRD with constant luminosity, in contrast to the wind velocity which scales with the stellar escape velocity, i.e. with $(M/R)^{0.5}$, where M and R are stellar mass and radius, respectively. Thus the wind velocity increases by more than a factor of 100 during the entire post-AGB evolution (cf. Pauldrach et al. 1988; Pauldrach et al. 2004, and Fig. 2, right panels).

Because of the dominant influence of the wind velocity on the wind power we considered it worthwhile to correlate the rim velocities, V_{rim} , also with the actual stellar wind speeds. The result is displayed in Fig. 11. The stellar wind

velocities are taken from the recent analysis and compilation of FUSE and IUE P-Cygni line profiles by Guerrero et al. (2010). Usually, different ions give different answers, and the observed ranges of wind velocities are indicated in the figure by horizontal bars. Since wind speeds increase with distance from the stellar surface, we placed the object symbol at the high-velocity end of the respective velocity bar.

Figure 11 reveals indeed a strong correlation between rim expansion and wind velocity of the respective central star, proving thereby that it is the stellar wind power that supports the nebula matter against collapsing and also sweeps up shell matter into a rim which is then accelerated against the more slowly expanding ambient shell gas. The comparison with the predictions of the hydrodynamical model sequences already introduced in Sect. 3.1 is interesting: The models fully encompass the observations and show the same trend with increasing central-star wind velocity.

Our Fig. 11 is similar to Fig. 1 in Patriarchi & Perinotto (1991) but displays a much tighter correlation because we used only objects with well known structure and carefully determined expansion property. The sample of Patriarchi & Perinotto is quite inhomogeneous and contains also objects with Wolf-Rayet central stars. These are known to have much higher mass-loss rates at similar wind velocities than stars with normal, hydrogen-rich surface composition, i.e. about 10^{-7} – $10^{-6} M_{\odot} \text{ yr}^{-1}$ (cf., e.g., Marcolino et al. 2007, and references therein) as compared to about 10^{-9} – $10^{-8} M_{\odot} \text{ yr}^{-1}$. The rim velocities of PNe with Wolf-Rayet nuclei are thus higher for the same stellar temperature.

4.3 The combined evolution of rim and shell

We have proven observationally in the previous subsections that both the formation and evolution of the rims and shells occur quite independently from each other, but nevertheless there exists some sort of interaction: while the shell expands as given by the density profile of the ambient medium, the rim must expand into the ambient shell gas. Thus not only the velocities proper are of relevance, but also their differences or ratios, and a good theory should predict their correct variation with time/evolution.

For this reason we show the ratio $V_{\text{post}}/V_{\text{rim}}$ in Fig. 12 where we used again the stellar effective temperature as proxy of the evolutionary progress. This figure elucidates impressively how large the ratio between the fastest flow velocities within a nebula and the usually measured flow velocities of the rim can be: For very young objects, a ratio of even about seven is possible!¹⁰ There is, however, a significant evolution with effective temperature: The ratio $V_{\text{post}}/V_{\text{rim}}$ approaches values around 1.5 for PNe with the hottest central stars.

Figure 12 demonstrates again the close correspondence between theory and observations. One can state that our

¹⁰ Note that $\dot{R}_{\text{out}}/V_{\text{rim}}$ is even larger, viz. by about 25 % (cf. Fig. 6).

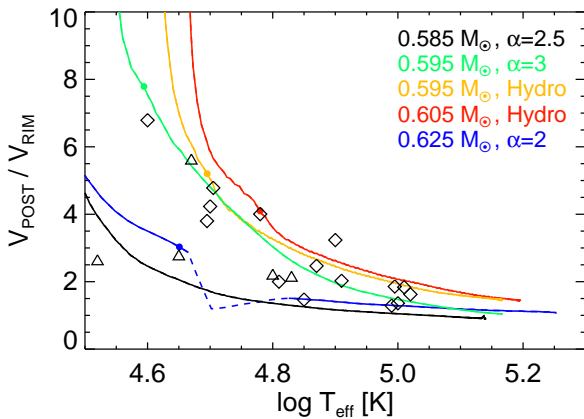


Fig. 12 The ratio of V_{post} and V_{rim} vs. stellar effective temperature, T_{eff} , for the objects of Table 1 and as predicted by the same hydrodynamical sequences as shown in Fig. 6 (see legend). Again, only the evolution towards maximum stellar temperature is of relevance. The optically thick/thin transition (if not outside the displayed range) is marked by a dot. Diamonds are for [O III] measurements, and triangles for [N II]. The dashed part of the $0.625 M_{\odot}$ sequence has the same meaning as in the previous figure.

radiation-hydrodynamics simulation based on debatable assumptions concerning, e.g., the stellar winds and initial configurations, give already a rather satisfying description of the real world.

5 Asymmetric expansion

Our precise measurements of rim (peak separation) and shell (post-shock) velocities revealed a fact that, to our knowledge, has not found attention so far: In several objects an asymmetry between the approaching and receding parts of the nebula is evident, in the sense that the differences between V_{rim} and V_{post} are not equal for both parts. A typical example with a rather obvious asymmetry is NGC 6826 whose [N II] and [O III] line profiles are displayed in Fig. 7. The differences between both velocities are 29 km s^{-1} for the receding nebular shell and 23 km s^{-1} for the approaching nebular shell, measured in the [O III] lines, a discrepancy of 6 km s^{-1} . Nearly the same value follows from the [N II] lines. It is also apparent from the line profiles of NGC 6826 that it is the stronger (receding) rim component that lags behind the expanding shell's shock, as compared to the weaker approaching rim component.

We defined an “expansion asymmetry”, ExpAs, as follows:

$$\text{ExpAs} = |(V_{\text{post}} - V_{\text{rim}})|_{\text{rec}} - |(V_{\text{post}} - V_{\text{rim}})|_{\text{app}}. \quad (1)$$

We defined also a “rim asymmetry”, RimAs, as

$$\text{RimAs} = A_{\text{rec}}/A_{\text{app}}, \quad (2)$$

where A is the emission-line area enclosed by the rim component resulting from our multi-Gaussian fit. The definitions (1) and (2) ensure that $\text{RimAs} < 1$ and $\text{ExpAS} < 0$

Table 2 Parameters describing the expansion asymmetry, RimAs and ExpAS, given by the average of N measured emission lines in [O III]. Values in parenthesis give the 1σ errors.

Object	RimAs	ExpAs (km s^{-1})	N
IC 3568	0.61 (0.11)	-5.9 (0.5)	4
M2-2	0.96 (0.09)	-5.1 (1.8)	8
NGC 3242	0.79 (0.05)	-2.4 (1.2)	8
NGC 6826	1.26 (0.05)	4.9 (0.5)	3
NGC 6891	2.06 (0.01)	2.7 (0.5)	2
Vy 2-3	0.51 (0.05)	-7.4 (0.2)	4

or $\text{RimAs} > 1$ and $\text{ExpAS} > 0$ if the PN side where the expansion of the stronger rim, V_{rim} , shows also a higher difference to V_{post} .

All objects for which we were able to see a measurable expansion asymmetry in their line profiles are compiled in Table 2, altogether 6 objects. We used data exclusively from [O III] because only this ensures an unambiguous determination of the strengths of the two rim components. The [N II] line profiles show generally stronger shell components which affects rather the strength than the position of the rim Gaussian.

Our measurements reveal that each of the six objects in Table 2 behave in the same way: The nebular side with the stronger rim component shows always the larger velocity difference to V_{post} than the weaker component. There is, however, not always a clear correlation between the size of both asymmetries. M2-2 has a strong expansion asymmetry, yet its rim asymmetry appears to be marginal. On the other hand, NGC 6891 shows one of the largest rim asymmetries, but only a rather modest expansion asymmetry.

Our interpretation of this phenomenon in terms of hydrodynamics and winds interaction is then the following: As noted in the introduction, the shell shock expands with a velocity \dot{R}_{out} according to the upstream density gradient and the electron temperature of the shell, but independently of the density itself. Since the upstream matter (i.e. the halo) is rather spherically distributed, as can be seen in Corradi et al. (2003) in general and in Schönberner et al. (2004) in particular for NGC 6826 (Fig. 4 therein), it is thus rather safe to assume that this PN expansion velocity \dot{R}_{out} is, to a first approximation, the same in all directions (at least for the objects considered here). The same holds then, of course, for the post-shock velocity. On the other hand, the rim is formed and accelerated by winds interaction, or more precisely, by compression of the inner shell gas by the expanding, wind-blown and shock-heated bubble. Any non-axisymmetric local inhomogeneities/differences of the gas densities in both shells along the line-of-sight must lead automatically to expansion differences between rim and shell of the receding and approaching parts of the PN, according to the work on interacting winds by Koo & McKee (1992).

The sometimes asymmetric expansion seen in some objects appears thus as a naturally consequence of the rather

inhomogeneous and non-spherical appearance of wind-blown/bubble-compressed rims seen in the images of most PN. We note that usually the PN's radial velocity is determined by centering the bright rim emission. If an expansion asymmetry exists for a particular object, the absolute mean radial velocity (but not the “expansion” velocity) can be wrong by up to a few km s^{-1} . Instead, centering the line emission using V_{post} , or the 10% level, would yield better radial velocities in these cases.

6 Evolved objects

Five objects from our target list, Hen 1-5, IC 1454, K 1-20, NGC 2438, and NGC 6894 do not belong to the group of younger middle-aged PNe with a clear double-shell structure and high-luminosity central stars and are not listed in the Tables 1 and A1. The shells of these objects are recombining/reionising because of low stellar temperature but still high luminosity (Hen 1-5) or low stellar luminosity and high stellar temperature (the other four objects). In such cases a clear interpretation of the line profiles in terms of rim and shell velocities is difficult.

The morphology of these objects (except Hen 1-5) is different from that of the usual double-shell PNe with luminous central stars.¹¹ The latter show a relatively small but bright rim with a large and faint (attached) shell which, because of its size, contains most of the ionised nebular mass (up to about 80%, depending on evolutionary stage). The situation is reversed in the evolved objects: The main body of the PN consists of a bright ring-like structure and an attached small, faint shell containing now obviously only a minor fraction of the whole nebular mass. This attached shell is usually at the 10% level, except for NGC 2438 where its brightness is at about 1% of the maximum value only (Fig. 3 in Corradi et al. 2000, henceforth Paper I).

The possibility of nebular recombination which may occur during the very rapid fading of hydrogen-burning central stars was recognised first by Tylenda (1986). He followed the expansion of simple, constant-density model nebulae coupled to evolving central-star models and described the ionisation/recombination fully time-dependently. Tylenda (1986) coined also the term “recombination halo” although it was the nebular shell, or part of it, that faded to halo brightness due to recombination. He provided a candidate list of objects which are supposed to be in the recombination/reionisation stage, and two of our targets (NGC 2438 and NGC 6894) are on that list.

6.1 Model simulations

Of course, our hydrodynamical simulations cover the phase of recombination/reionisation as well in a fully time-dependent fashion, and they were already extensively used

in a study of NGC 2438 in Paper I. There we put our emphasis on the development of surface brightnesses during recombination/reionisation, but here we will concentrate on the signatures of the different line profiles ([N II] vs. [O III]).

We show in Fig. 13 four snapshots of model structures taken from our hydrodynamical model sequence, beginning with the last model that has been shown and discussed in Paper I (Fig. A9 therein). This particular model depicts the situation during reionisation more than 5000 years after the beginning of strong recombination, and the following snapshots, not discussed in Paper I, illustrate the model evolution for about further 1921 years of evolution.

Recombination is, of course, not total, i.e. the recombination “front” does not reach the bubble/rim interface, although it may penetrate well into the rim. At some radial position, however, the local rates of recombination and ionisation become equal, and because of the continued expansion, this point will soon move again outwards, i.e. a reionisation “front” expands while more distant regions are still recombining.¹² Positive density and velocity gradients are soon established again, in conjunction with a strong ionisation stratification, as is similar for young, still optically thick PNe. Thus, N^+ traces the outer parts of the (re)ionised shell, close to a newly created leading shock/ionisation front where the flow velocity is high ($\sim 40 \text{ km s}^{-1}$), while O^{++} traces preferably the inner parts where the flow velocity is lower. In particular, the inner, strong peaks of the [O III] profile corresponds to a newly forming shell of weakly compressed gas, i.e. a “new” rim (cf. lower right panels in the individual snapshots of Fig. 13) which expands with about 20 km s^{-1} only.

Line profiles and intensity distributions seen in the left panels of the individual frames of Fig. 13 reflect the quite extreme ionisation stratification in the models. In projection, the models appear as broad ring-like structures in the light of $\text{H}\beta$ and [O III], but as much narrower ones in [N II]. Correspondingly, the [O III] line is broad and covers nearly the whole velocity range of the reionised shell. Typically is a double-peak structure caused by the influence of the radial profiles of O^{++} ion density and flow velocity in conjunction with projection effects. The relative strengths of these [O III] subcomponents change during evolution, reflecting obviously the change of the density profile in that part of the model nebula where O^{++} is present, while the velocity gradient remains similar. In contrast to [O III], the [N II] line has always no structure, is very narrow and traces the fastest flowing matter immediately behind the new shock.

The “old” leading shock of the former shell, now being mostly neutral, is still moving ahead but with lower speed. Its position is marked in all snapshots by a sharp temperature spike, moving from 14×10^{17} to 16×10^{17} cm at the last snapshot. As evolution progresses, reionisation passes this old shock, and the former fairly neutral shell becomes visible in, e.g. $\text{H}\alpha$ (or $\text{H}\beta$) and [N II] (left bottom panel of

¹¹ Images of these objects, next to others, can be found in <http://www.astro.washington.edu/users/balick/PNIC/>.

¹² The less dense halo gas ahead of the “old” shock usually remains at a much higher degree of ionisation because of its lower recombination rates.

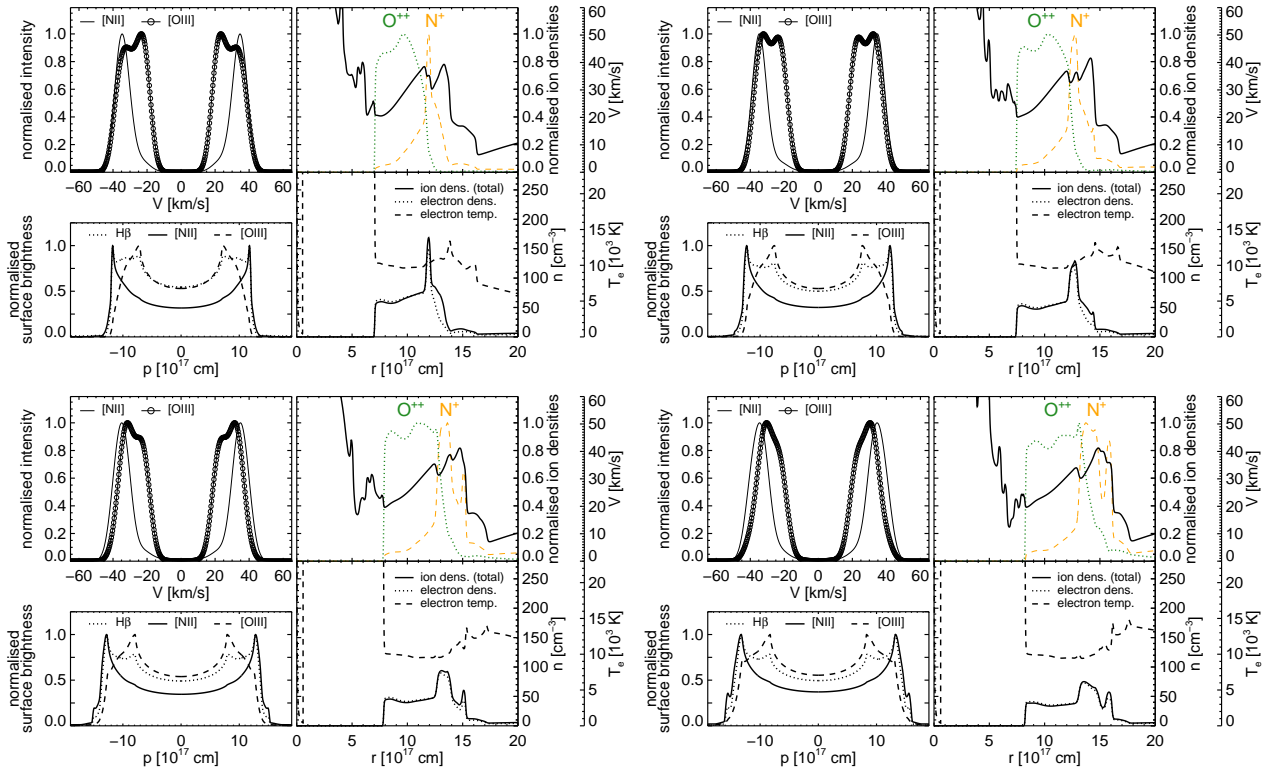


Fig. 13 Snapshots of four model structures and respective line and intensity profiles during the post-recombination stage of evolution, taken from our hydrodynamical model sequence with a $0.605 M_{\odot}$ central star. The models cover a total time span of 1921 years of evolution. The model parameters are as follows: *Top left*: $L = 215 L_{\odot}$, $T_{\text{eff}} = 120\,370$ K, at post-AGB age $t = 13\,136$ yr, corresponding to Fig. A9 of Paper I; *top right*: $L = 211 L_{\odot}$, $T_{\text{eff}} = 120\,117$ K, at post-AGB age $t = 13\,778$ yr; *bottom left*: $L = 206 L_{\odot}$, $T_{\text{eff}} = 119\,814$ K, at post-AGB age $t = 14\,419$ yr; *bottom right*: $L = 202 L_{\odot}$, $T_{\text{eff}} = 119\,453$ K, at post-AGB age $t = 15\,057$ yr. The content of each snapshot is the following: *Top left panels*: normalised line profiles of [N II] (thin solid) and of [O III] (connected circles). The [N II] line is stronger than the [O III] line by factors of about 2–4, depending on the model. The spectral resolution corresponds to 6 km s^{-1} in all cases. *Bottom left panels*: normalised surface brightness profiles for H β (dotted), [N II] (solid), and [O III] (dashed). *Top right panels*: the velocity field together with the (normalised) ion densities of N^+ and O^{++} . *Bottom right panels*: heavy particle density (solid), electron density (dotted), and electron temperature (dashed) vs. radius. The PN model proper of each snapshot is confined by the contact discontinuity (density jump at the inner PN edge) which propagates from 7 to 8×10^{17} cm during the 1921 years shown here, and the position of the “old” leading shock (sharp temperature spike) propagates from 14 to 16×10^{17} cm in the same time. The new shock/reionisation front is at 12×10^{17} cm (*top left*), progresses to 13×10^{17} cm (*top right*), but then the reionisation “front” is passing the old shock between the *bottom left* and *bottom right* snapshots, leaving the new shock behind (at 15×10^{17} cm, *bottom right*).

left bottom frame in Fig. 13, between $r = 14 \times 10^{17}$ cm and 15.5×10^{17} cm). The intensities of this “rekindled” attached shell is between 20 and 10% of maximum nebular emission, in fair agreement with the images of IC 1454, NGC 6894, and K 1-20. NGC 2438 constitutes obviously an earlier phase of evolution in which the old shell is still mostly neutral and thus “invisible”. It is interesting to note that the signature of this rekindled shell is not seen in the theoretical line profiles of Fig. 13 (bottom frames). The reason is simple: the shell is faint, and its flow velocities are too close to those behind the new shock.

Our models show that reionisation fronts are not very sharp. The low densities ($\approx 100 \text{ cm}^{-3}$) in combination with the free path lengths of the very abundant high-energy photons emitted by the hot central star ($\approx 120\,000$ K) lead to a

more gradual decrease of the degree of ionisation with distance. This can be seen by the run of the electron density (dotted) between 12×10^{17} and 15×10^{17} cm in the lower right panels of the two upper frames of Fig. 13.

The model simulations predict also that the reionisation stage is long-lasting: For the sequence shown in Fig. 13, reionisation started about 5000 years ago and is still continuing: In the last model shown in Fig. 13, about 7000 years after recombination, $\approx 20\%$ of hydrogen behind the old shock is still neutral. Even about 4500 years later, at $t = 19\,480$ yr, there is about 6% neutral hydrogen left. In contrast, recombination occurred on a much shorter time scale: within only less than 1000 years for the simulations shown in Fig. 13. We emphasise here that *recombination and reionisation may occur at the same time but in differ-*

ent regions of a PN. For instance, by comparing Figs. A2, A3, and A4 in Paper I one sees that, while the shell is still recombining, the old rim changes into a density structure which is typical for reionisation.

Whether the new shock, created by reionisation, will merge with the old one depends entirely on their further velocity evolution. The last computed model with $t = 19\,480$ yr (not shown) has still two outer shock fronts, the old one at $r = 20 \times 10^{17}$ cm and the new one at 18×10^{17} cm, both propagating with nearly the same speed.

We noted already that the situation during reionisation as depicted in Fig. 13 is similar to the earliest, optically-thick phase of nebular evolution. There is, however, an important difference: In young PNe the central star is cool, and hence N^+ constitutes a major ionisation stage throughout the whole nebula, while O^{++} is confined only to the inner region close to the star. Here, the central star is very hot, and the situation is reversed: O^{++} is a major species, and N^+ is only present close to the reionisation front.¹³

6.2 Observations and their interpretation

The central line-of-sight profiles extracted from the spectrograms of our five targets are displayed in Fig. 14. The profiles appear quite noisy, even after averaging along dispersion over several pixel rows. Despite this noise there appears a marked difference between these profiles and the ones discussed earlier in this paper. The individual [O III] shell components are broad and often split while the corresponding [N II] line components are narrower and *always* unsplit. From the total line split follows that maximum flow velocities must be in all cases quite high, ranging from 30 km s^{-1} (Hen 1-5) up to over 50 km s^{-1} (IC 1454).

We will discuss and interpret the line profiles of these five objects in turn in the following paragraphs.

Hen 1-5 This object is a singular case in our sample: Its central star, FG Sge, obviously recovering from a late thermal pulse during the transition from the tip of the AGB to the white dwarf domain, is now a cool object, a so-called “born-again” giant with $T_{\text{eff}} \simeq 5500 \text{ K}$ (Blöcker & Schönberner 1997; Jeffery & Schönberner 2006). Without any ionising source for about 130 years, the nebular shell must be fairly well recombined.

We measured from our [N II] profiles a peak-to-peak separation of $30 \pm 3 \text{ km s}^{-1}$, in good agreement with the determination of Flannery & Herbig (1973). The $H\alpha$ line at our disposal is very similar, which indicates that both H^+ and N^+ are tracing the same still partly ionised region. A more thorough discussion cannot be done here because such an evolutionary stage is not covered by our models.

¹³ The same situation holds, of course, for the relation between O^+ and O^{++} .

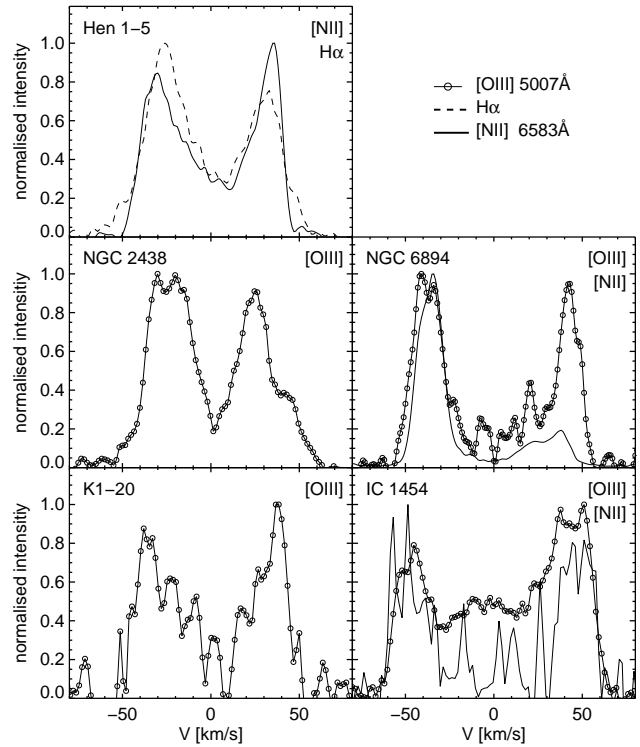


Fig. 14 Central line-of-sight profiles of 5 evolved objects, Hen 1-5 (top left), NGC 2438 (middle left), NGC 6894 (middle right), K 1-20 (bottom left), and IC 1454 (bottom right) which are not contained in the sample listed in Table 1. All profiles are normalised at their maximum strength; solid for [N II], dashed for $H\alpha$, and connected circles for [O III]. The profiles of K 1-20 and IC 1454 are averaged over 7 pixel rows for improving S/N.

NGC 2438 This object shows a bright, ring-like and somewhat diffuse main shell, attached with two round halo-like structures, placing this object into the small group of PNe with apparently two halos (cf. Corradi et al. 2003). It is debated whether the inner halo-like structure is just the faint remnant of the shell which suffered from severe recombination (Paper I) or a real halo (Rauch et al. 1999; Dalnódar 2012). The central star of NGC 2438 is very hot ($\simeq 140\,000 \text{ K}$) and faint ($\simeq 160 L_{\odot}$, Malkov 1997), a fact that makes the recombination scenario quite plausible.

Because there exists the possibility that a more detailed velocity information may help in clarifying the status of NGC 2438, we took additional spectrograms by placing the slit right in the middle of the bright [O III] “ring”. We will discuss and interpret the resulting line profiles in turn.

The central profile of the [O III] line is seen in Fig. 14, middle left. The total peak-to-peak separation corresponds to a flow expansion velocity of about 30 km s^{-1} . However, the approaching component shows an unusual feature: It is split into two subcomponents separated by about 14 km s^{-1} , and the whole appearance of this component is very similar to theoretical profiles shown in Fig. 13 which have, in some

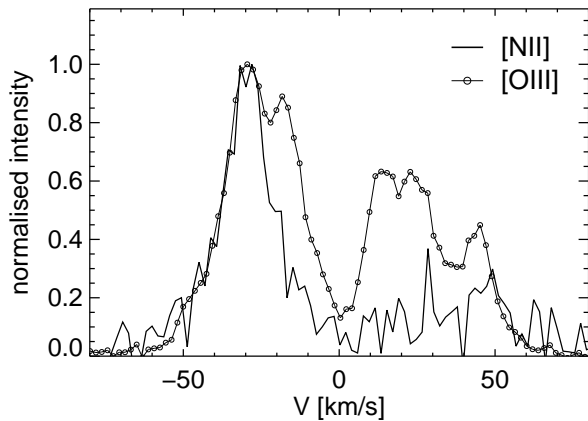


Fig. 15 Central line-of-sight line profiles (normalised) of [N II] and [O III] as extracted from the long-slit spectra of NGC 2438 presented in Fig. 2 of Paper I. The profiles are averaged over 5 ([N II]) and 3 ([O III]) pixel rows, resp.

cases, components clearly split by about 10 km s^{-1} , too (cf. top right frame of Fig. 13). Additionally, there appear weak shoulders (mainly for the receding part) suggesting expansion flow velocities up to about 50 km s^{-1} .

Since no [N II] profile from Tautenburg Observatory is at our disposal, we employed long-slit spectrograms taken at the 3.5 m NTT telescope of ESO and already discussed in Paper I. The central profiles of both [N II] and [O III] are shown in Fig. 15. The better spectral resolution of the NTT spectrogram reveals that also the [O III] component of the receding shell is split. The velocity range within the (re)ionised shell as measured by this line split extends from about 17 km s^{-1} (from the separation of the inner [O III] line peaks seen in Fig. 15) to a velocity of at least 26 km s^{-1} (from the separation of the outer [O III] components).¹⁴

The [N II] line component (approaching shell only) is single and its velocity position coincides, as predicted by our models in Fig. 13, with the corresponding outer [O III] component. In the receding shell N^+ is obviously absent, indicating a possibly higher stage of (re)ionisation. In this part of the shell we see in [O III] also significant emission at flow velocities between about $40\text{--}50 \text{ km s}^{-1}$, corresponding to the shoulder present in our Tautenburg spectrogram (cf. Fig. 14, middle left). Such velocities are only marginally seen in the approaching part of the nebula. It is tempting to identify this flow signature as belonging to the old shell now being reionised in the direction of the central line-of-sight. We have seen earlier in Sect. 3 that the PN shells attain such high flow velocities (post-shock velocities) during the end of the horizontal evolution across the HRD.

Such a strong line strength difference between approaching and receding parts of the nebula (also seen in NGC 6894, cf. below) is quite unusual during the evolution

¹⁴ More precisely, the velocity range extends to about 30 km s^{-1} since the post-shock velocity is not traced by the line peak, as judged from our models shown in Fig. 13.

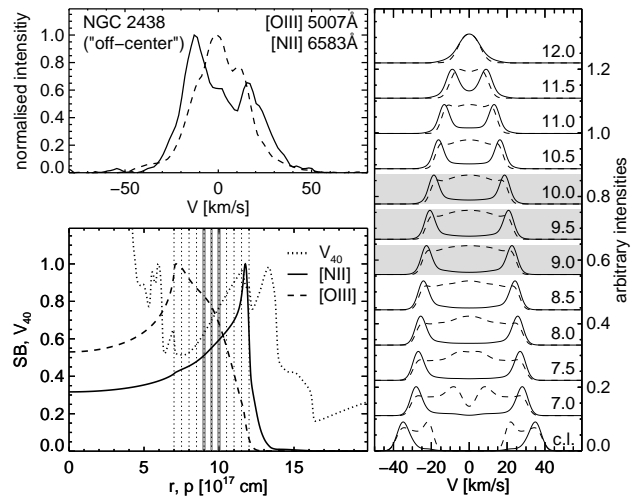


Fig. 16 Line profiles of NGC 2438 taken at the radial position of the bright ring and their interpretation by the hydrodynamical model shown in Fig. 13, top right. *Top left*: observed profiles of [N II] (solid) and [O III] (dashed). *Bottom left*: modelled normalised surface brightness profiles of [N II] (solid) and [O III] (dashed), and the flow velocity in units of 40 km s^{-1} (dotted). Vertical lines (thick gray and dotted) indicate the radial positions of the numerical slit with width of $2 \times 10^{16} \text{ cm}$. *Right*: normalised line profiles of [N II] (solid) and [O III] (dashed) as computed from the model. The numbers ($\times 10^{17} \text{ cm}$) at the individual profiles correspond to the radial positions of the numerical slit belonging to the respective profiles. The bottom profiles are for the central line-of-sight (cf. top left panel of top right snapshot in Fig. 13). The profiles underlaid by a grey shade belong to the slit positions marked in thick grey in the *bottom left* panel which correspond closely to the slit position used for the observations.

prior to recombination. Here, however, the reionised shell is shaped out of the already “patchy”/inhomogeneous rim material, and this fact is most likely the cause of the now very asymmetrical appearance of the line profiles.

If the bright ring of NGC 2438, as seen in projection onto the plane of sky, has indeed a positive velocity gradient combined with an ionisation stratification as it is typical for the stage of reionisation, line profiles taken at a position centred on this ring should reflect this fact: Both components should be split/structured, at least in [N II] because N^+ is concentrated only at the outer edge of the reionised shell.

A comparison between the observation and theoretical prediction is depicted in Fig. 16. Indeed, the observed line profiles of [N II] and [O III] correspond to our expectations: The [O III] line is unsplit, but with shoulders, whereas the [N II] line is split, and its peak-to-peak separation corresponds closely to the shoulders of the [O III] line (top left panel of Fig. 16). The [N II] peak separation, $2 \times 15 \text{ km s}^{-1}$ corresponds, if the projection effect is taken into account, to a central line-of-sight separation of about $2 \times 27 \text{ km s}^{-1}$, in

fair agreement with the central line-of-sight measurement ($2 \times 30 \text{ km s}^{-1}$).

The bottom left panel of Fig. 16 renders the intensity profiles in [N II] and [O III] together with the positions of the numerical slits used for the computation of the profiles seen in the right panel. The radial gas velocity distribution is shown as well. These line profiles, and the intensity profiles as well, are the consequence of the ionisation stratification of the reionising model, as is evident by the very different intensity profiles of [N II] and [O III] in combination with the positive velocity gradient (cf. top right frame of Fig. 13). The shaded part highlights those modelled profiles with the closest similarity to the observed ones.

We state that the nebular model presented in this figure provides a satisfactory description of the evolutionary stage of NGC 2438. The observed line profiles (together with the surface brightness profiles shown in Fig. 3 of Paper I) can be interpreted such that the shell of NGC 2438 has experienced a rather strong recombination in the very recent past and that the object is now in the slow phase of reionisation due to the continuing expansion. NGC 2438 seems to be in a quite early phase of reionisation because its former (attached) shell is still very faint, i.e. must still be quite neutral (cf. top left frame of Fig. 13).

The recently measured high electron temperature beyond the boundary of the bright ring (rim), i.e. beyond the reionisation front (Dalnodar 2012), is not in contradiction to this statement as our models show (bottom right panel in the top left frame of Fig. 13): Despite its still lower degree of ionisation, the upstream region of the reionisation shock at $12 \times 10^{17} \text{ cm}$ is even hotter than the fully reionised regions behind (about 11 000–12 000 K versus about 10 000 K). The reason is heating beyond the reionisation front proper by the most energetic photons which also have the highest free path lengths. Our model prediction is fairly consistent with the Dalnodar measurement of about 15 000 K versus 10 000–12 000 K in the bright ring.

NGC 6894 The image of this object displays a bright, round inner structure with a hardly to be seen (attached) shell. It is a typical very far evolved object supposed to be in the recombination/reionisation stage as well with a central star of $T_{\text{eff}} \simeq 120\,000 \text{ K}$ and $L \simeq 120 L_{\odot}$ (Malkov 1997).

The [O III] line component of the approaching shell is clearly split, but by only about 9 km s^{-1} . Again, the corresponding [N II] is not split (Fig. 14). Here, however, the [N II] line-peak position corresponds to the inner [O III] component (cf. explanation below). We can only estimate the flow velocity close to the edge of the reionised shell from the total [O III] line separation, 42 km s^{-1} , in good agreement with the entry in Weinberger’s catalogue (Weinberger 1989) of 43 km s^{-1} .

The velocity range within the (re)ionised shell is smaller than that in NGC 2438, which is clearly seen by the different spacings of the split [O III] lines: $\simeq 9$ vs. $\simeq 14 \text{ km s}^{-1}$

(Fig. 14). The corresponding line split for the model rendered in Fig. 13 is 25 km s^{-1} (top frames).

It appears surprising and not in line with our model predictions that the [N II] peak separation gives a lower velocity than [O III] (cf. Fig. 14, middle right, $\simeq 38$ vs. 42 km s^{-1}). We must state, however, that the [O III] and [N II] spectrograms are taken on different days. Given the high expansion velocity and the nebula’s moderate apparent size, already a small difference in slit position might lead to a measurable velocity separation.

K 1-20 K 1-20 is an object with a very low surface brightness and appears on the sky as a broad ring with an attached shell (cf. Guerrero et al. 1998). According to Górný (priv. comm.), the central star is very faint ($< 100 L_{\odot}$), too. Our noisy [O III] line profile indicates, from the peak separation, flow velocities up to about 40 km s^{-1} , in very good agreement with the result of Guerrero et al. (1998) from their [N II] measurements.¹⁵

IC 1454 IC 1454 (= A 81) is another far evolved object with a very hot but faint central star ($L \approx 150 L_{\odot}$, Górný, priv. comm.). The image consists of a wide, bright rim-like structure with a small attached shell as well. Our [O III] line profile shown in Fig. 14 (bottom right) is rather noisy, but appears to have the (expected) double components, with a split of about 10 km s^{-1} . The total line separation corresponds to a radial flow velocity up to at least 50 km s^{-1} . Our extremely noisy [N II] spectrogram is consistent with such high velocities.

Our measurement is in fair agreement with the corresponding entry in Weinberger’s catalogue (46 km s^{-1} from the [O III] peak separation; Weinberger 1989). An “expansion” velocity as low as 20 km s^{-1} , as advocated by Guerrero et al. (1998), is not confirmed.

6.3 Remarks

We note here that recombination, if it occurs at all, is only a transient phenomenon during the total life of a PN, and that a PN does not become “extinct” by recombination because the latter never progresses towards the innermost regions of a PN where the radiation field even of a low-luminosity central star is sufficient to keep up ionisation. Rather, expansion continues, accompanied by reionisation, until the PN’s surface brightness becomes too low for detection. The final reionisation phase of nebula evolution is characterised by strong ionisation stratification, resulting in smaller peak-separation velocities for [O III] as compared to [N II] (see Fig. 13), at least temporarily. Velocities based on [O III] alone would then suggest a nebular deceleration (Pereyra et al. 2013) which, however, is not real.

We note also that all five objects investigated here expand rather fast ($> 40 \text{ km s}^{-1}$ post-shock velocity, except

¹⁵ The authors list $39 \pm 3 \text{ km s}^{-1}$ in their Table 4, but the corresponding échelogram is not presented in their Fig. 1.

Hen 1-5), which is comparable to the phases of evolution immediately prior to recombination (cf. Fig. 9). This is somewhat surprising since the common belief is that, once the central star has faded, the nebular expansion will slow down (cf., e.g., discussion in Pereyra et al. 2013). Indeed, our model calculations show that the “old” leading shock decelerates during recombination, but due to reionisation a new shock is created further inwards, starting with a propagation velocity based on that of the rim matter, i.e. of about 30 km s^{-1} (instead of $10\text{--}15 \text{ km s}^{-1}$ during the “first” ionisation). This new shock can therefore easily be accelerated to about 50 km s^{-1} during reionisation, and it will merge eventually with the old shock, maintaining its high velocity.

We emphasise that recombination/reionisation as discussed here is only an issue if significant parts of the nebula recombine. Only then a new shock is created which leads the expansion of the reionised shell. Thus this phenomenon is restricted to more massive central stars that evolve fast enough such that the nebula is still sufficiently dense to allow for severe recombination during stellar fading. The sequence shown in Fig. 13 describes the case of rather strong recombination.

Another interesting aspect of fast expanding nebulae around evolved, very faint central stars is worth noting: These objects are in a phase of very weak or maybe even nearly absent stellar winds, yet they expand very fast. Hence interacting winds cannot be responsible for this expansion! We conclude again that it is exclusively the thermal pressure gradient established by excessive gas heating during the process of reionisation. Indeed, the models shown in Fig. 13 reveal a very slow expansion of the hot bubble of less than 20 km s^{-1} only, which is clearly not enough to compress the inner gas shells into a rim as is seen in the younger nebulae, not to speak of accelerating the rim matter to the observed high velocities.

In this context we note that the close resemblance of our theoretical line profiles with the observations indicates that the hot bubbles must not necessarily collapse in reality, at least for the objects investigated in this work. This implies that, as assumed in the modelling, the central-star (or hot white dwarf) is still able to sustain a wind sufficiently strong not only for preventing the collapse of the bubble but also for keeping up a slow expansion of the bubble.

7 Expansion and metallicity

Thanks to the spatial and spectral resolution capability of the FLAMES/ARGUS IFU at the VLT, we were able to determine separate velocity information for the rims and shells for a sample of four metal-poor PNe. We analysed the line profiles in the same way as for the Galactic disk objects, and the results are presented in the following.

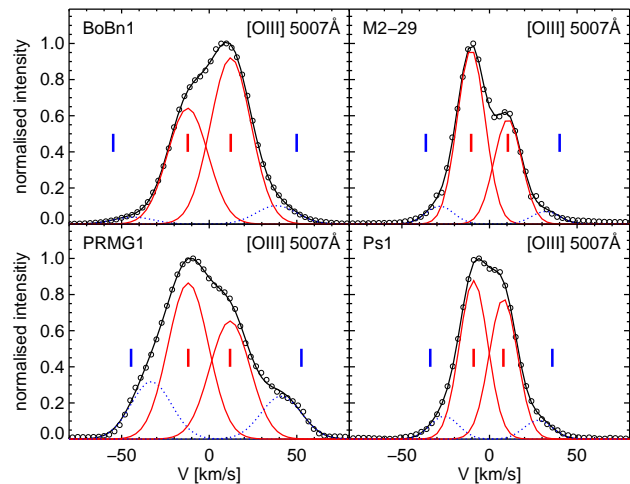


Fig. 17 Central line-of-sight line profiles of [O III] 5007 \AA for four metal-deficient PNe observed by us with VLT FLAMES /ARGUS and their decompositions into four Gaussians. The two rim Gaussians (red solid) are forced to have the same half widths, and the post-shock velocities are marked, too. The latter are based on the sigmas of the respective Gaussians, except for PRMG 1 where the derivative method could be applied.

Table 3 Values of measured rim and post-shock velocities deduced from the line profiles of [O III], oxygen abundances (Col. 4) and stellar temperatures (Col. 5), both from Howard et al. (1997), and additional stellar temperature information (Col. 6) from Malkov (1997).

Object	V_{rim} [km s^{-1}]	V_{post} [km s^{-1}]	$12 + \log(\text{O}/\text{H})$	$\log(T_{\text{eff}}/\text{K})$	$\log(T_{\text{eff}}/\text{K})$
BoBn 1	12	52	7.83^3	5.10^3	4.98
M2-29	10	38	7.71^1	4.86^1	4.70
PRMG 1	12	49	8.06	5.01	4.91
Ps 1	8	35	7.61	4.66^2	4.59

Notes: All velocities are based on one spectrogram only, hence individual velocity errors are estimated to $\pm 2 \text{ km s}^{-1}$ for V_{rim} and $\pm 3 \text{ km s}^{-1}$ for V_{post} .

¹ Miszalski et al. (2011) determined $T_{\text{eff}} = 50 \pm 10 \text{ kK}$ for the central star of M2-29 from detailed matching of photospheric lines by means of NLTE model atmospheres and a nebular oxygen abundance of $12 + \log(\text{O}/\text{H}) = 8.3$ from the nebular lines.

² Heber, Dreizler & Werner (1993) determined $T_{\text{eff}} = 37 \text{ kK}$, Rauch, Heber & Werner (2002) $T_{\text{eff}} = 39 \text{ kK}$.

³ According to Otsuka et al. (2010), $\log T_{\text{eff}} = 5.10$ and $12 + \log(\text{O}/\text{H}) = 7.74$.

7.1 Our sample of metal-deficient PNe

The results of the line analyses of the four metal-poor objects are illustrated in Fig. 17. All profiles appear nearly resolved, allowing a measurement of the rim velocities which are similar and around 10 km s^{-1} for all four objects. Also, in all cases weak but somewhat extended shoulders are visible, allowing in each object a firm determination of the

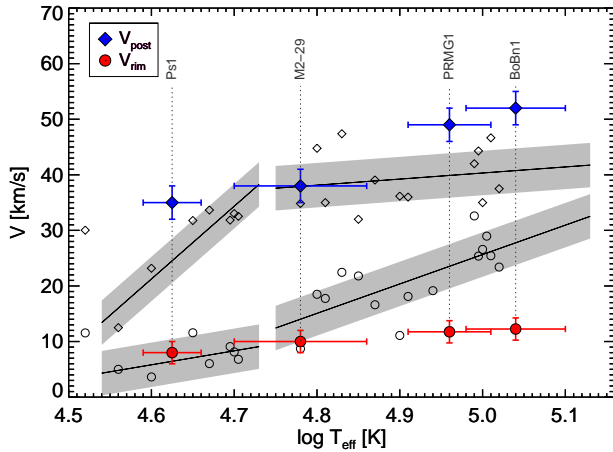


Fig. 18 Positions in the $T_{\text{eff}}-V$ plane of our metal-poor PNe, with horizontal bars, indicating the range of temperature determinations (cf. Table 3). The general run of the velocities with effective temperatures for the PNe in the Milky Way disk are shown in a schematic way as well. The objects from Fig. 9 are underlaid as small open diamonds and circles.

shell’s post-shock velocity, either by a Gaussian decomposition or the derivative method (PRMG 1 only).

Our velocity measurements are listed in Table 3, together with the objects’ oxygen abundances and stellar effective temperatures, both taken from Howard et al. (1997), for consistency. For comparison, values from other sources are mentioned as well. The positions of these four metal-poor objects in the $T_{\text{eff}}-V$ plane is, together with our sample of Galactic disk objects (from Fig. 9), also illustrated in Fig. 18. Despite the considerable uncertainties of the stellar temperatures (except for Ps 1), the following facts are noticeable:

- Ps 1 with about 1/10 of solar oxygen is a young object with a cool central star, yet its V_{post} is with 42 km s^{-1} unusually high.
- BoBn 1 and PRMG 1 are less depleted in oxygen and have hot central stars, i.e. they are the most evolved objects in our sample. Yet both have a very low rim velocity ($V_{\text{rim}} = 12 \text{ km s}^{-1}$), but their post-shock velocity of about 50 km s^{-1} is above the upper boundary for Galactic disk objects with similarly hot central stars.
- M2-29 is obviously a middle-aged PN with a V_{rim} at the lower boundary compared to the Galactic disk PNe. Its V_{post} (38 km s^{-1}) is still well within the range of typical values for Galactic disk PNe.

The four objects with metal-poor composition analysed here comply perfectly with the expectations from theory, as outlined in the Introduction and in more detail in Schönberner et al. (2010). Although the initial rim expansion can be assumed to have been about the same as in metal-rich objects (close to the original AGB-wind speed), there is hardly any further rim acceleration with increasing stellar temperature which is obviously evidence for a

rather weak stellar wind, certainly a consequence of the low metallicity. On the other hand, the velocities of the shells’ outer edges are just as high or even higher than those of Galactic disk objects with similar evolutionary state, reflecting the higher electron temperatures caused by the reduced line cooling: The nebular electron temperatures range from $13\,000 \text{ K}$ for the young PN Ps 1 to about $15\,000\text{--}16\,000 \text{ K}$ for the evolved PNe PRMG 1 and BoBn 1 (Howard et al. 1997). For comparison, the electron temperatures for the Galactic disk PN sample in our Table 1 range from about 8000 K up to about $12\,000 \text{ K}$ for the most evolved objects.

7.2 Velocities from the literature

Other measurements of “expansion” velocities of metal-poor objects are rare. We restrict our comparison to those measurements only that are based on spatial and/or spectroscopic resolutions similar to ours.

BoBn 1 Otsuka et al. (2010) observed BoBn 1 with Subaru/HDS and used archival data from VLT/UVES for a detailed chemical and kinematical analysis. The line profiles appear hardly resolved (see their Fig. 5). A two-component Gaussian decomposition of [O II] yields, in their notation, $V_{\text{exp}} = 16 \text{ km s}^{-1}$, while we found $V_{\text{rim}} = 12 \text{ km s}^{-1}$ (see Table 3). From the half widths of the unresolved lines the authors estimated expansion velocities up to about 30 km s^{-1} , well below our value for the post-shock velocity of 52 km s^{-1} . Using, however, the 10%-level of the line profiles of ions with medium degree of ionisation, velocities of $40\text{--}45 \text{ km s}^{-1}$ can be estimated from their figure, much closer to V_{post} as derived here.

M2-29 Gesicki et al. (2010) analysed the same data that we used here, but unfortunately they are not showing any line profiles. Instead, they present only position-velocity diagrams with isophotes which render a detailed comparison impossible. Still, the authors combined line profiles with a radial density profile derived from the nebula’s intensity distributions (in the 1D approach) for determining the radial velocity field: Their best fit is a constant velocity of 12 km s^{-1} plus an additional turbulent velocity component of 7 km s^{-1} which is necessary to fit the line wings.

Given the physics of expanding shock waves, a radially constant velocity field is unphysical. Also the introduction of a turbulent velocity field with amplitudes of the same order as the general flow speed and encompassing the entire nebula appears to us as an unphysical approach as well. The value of 12 km s^{-1} , however, is consistent with our measurement of $V_{\text{rim}} = 10 \text{ km s}^{-1}$, but the wings of the [O III] profile shown in Fig. 17 (top right) are certainly the signature of an attached shell with a positive velocity gradient and a rather high post-shock velocity (38 km s^{-1} , cf. Table 3).¹⁶

¹⁶ The nebular model of Gesicki et al. (2010) consists of a dedicated structure, i.e. of a dense inner rim and a very faint attached shell, mainly visible in [N II] (cf. their Fig. 7). Given an electron temperature of

Miszalski et al. (2011) redetermined the nebular abundances and found only a mild metal deficiency (e.g. $12 + \log(\text{O}/\text{H}) = 8.3$), not enough to justify a halo classification. Together with a distance estimate of 7.7 kpc and the coordinates they concluded that M2-29 belongs to the Milky Way bulge, although its chemical abundances are a bit below typical bulge values (see Table 6 in Miszalski et al. 2011). The only modest metal deficit explains our measurement of the shell's post-shock velocity, the lowest of all the four objects listed in Table 3 and in fair agreement with typical values for Galactic disk objects at the same evolutionary state (Fig. 18).

With known distance and a set of “expansion velocities” it appears interesting to discuss their relevance for an estimate of the object's post-AGB age. With distance to the bulge (centre) and angular size of the object ($4''.9$), a nebular radius of 2.8×10^{17} cm (0.09 pc) follows. Hence a kinematical age of 2300 years is derived from simply applying $R_{\text{out}}/V_{\text{post}}$ and using our measurement of $V_{\text{post}} = 38 \text{ km s}^{-1}$. The real post-AGB age is higher because (i) the transition time and (ii) the nebular acceleration must be considered (cf. Sect. 1.3): From our hydrodynamical models we estimate an age increase of up to 40%, i.e. to a (reasonable) post-AGB age of up to 3300 years, depending on the model used (cf. Fig. 5). With an expansion speed of only 12 km s^{-1} , as advocated by Gesicki et al. (2010), the post-AGB age would be about three times higher, viz. about 10 000 years. The possible central-star mass range given by Miszalski et al. (2011), $0.6_{-0.10}^{+0.28} M_{\odot}$, is very large and accommodates (theoretical) post-AGB ages from a few hundreds to up to more than 100 000 years (cf. Blöcker 1995).

Ps 1 Bianchi et al. (2001) measured for Ps 1 an “expansion” velocity of 12 km s^{-1} from the HWHM of high-resolution [N II] lines, which corresponds to our $V_{\text{rim}} = 8 \text{ km s}^{-1}$ result gained from the decomposition of the [O III] line (cf. Table 3). More recently, Tajitsu & Otsuka (2006) observed Ps 1 with the High Dispersion Spectrograph of the 8.2 m Subaru telescope. Their central line-of-sight profile is very similar to ours (see Tajitsu & Otsuka 2006, their Fig. 1), and the authors were able to resolve the [O III] profile into four Gaussian components: in two strong, inner components separated by 15 km s^{-1} and two faint outer ones separated by about 60 km s^{-1} . The latter were called “high-velocity components” pointing in opposite direction in the line-of-sight. Our interpretation is that these high-velocity components are nothing else but the signature of the faint outer shell seen in the image of Ps 1. They appear much stronger in [N II] (see again Tajitsu & Otsuka 2006, bottom left of their Fig. 1), which is typical for the [N II] emission from nebulae with still cooler central stars.¹⁷

10 000 K, an AGB-wind velocity of 10 km s^{-1} , and an AGB-wind density profile that can be described by an $r^{-\alpha}$ profile with exponent $\alpha = 2$, the shell's post-shock velocity must already be at 20 km s^{-1} . With a more realistic $\alpha = 3$ value, a post-shock velocity between 30 and 40 km s^{-1} follows (cf. Fig. 10, top panel).

¹⁷ An example is seen in Fig. 7 for the case of NGC 6826.

Extracting the Gaussians given in Fig. 1 of Tajitsu & Otsuka (2006), we found from the [O III] profile $V_{\text{rim}} = 8 \text{ km s}^{-1}$ (from the strong inner components) and $V_{\text{post}} = 31 \text{ km s}^{-1}$ from the outer, faint shell components. The [N II] profile is centrally unresolved, but from the outer Gaussian components we extracted $V_{\text{post}} = 36 \text{ km s}^{-1}$. Altogether we have excellent agreement between our results gained from FLAMES/ARGUS observations with the Subaru observations of Tajitsu & Otsuka (2006).

Ps 1 is a member of M 15, hence its distance is well-known. We adopt here a distance of 10.2 ± 0.4 kpc, the mean of the two most recent dynamical distance determinations (McNamara et al. 2004; van den Bosch et al. 2006). The observed nebular dimension of $3''.1 \times 2''.7$ (Alves, Bond & Livio 2000) results in a mean shell radius of 0.07 pc, and combined with $V_{\text{post}} = 35 \text{ km s}^{-1}$, a kinematic age of about 1900 years follows.

The real, i.e. post-AGB age, is difficult to estimate since Fig. 5 does not contain fast accelerating metal-poor models around low-mass central stars.¹⁸ It is clear that a rapid increase of shock speed following the rather long transition phase during which the inner edge of the AGB wind envelope expands with about 10 km s^{-1} leads to a large correction of the kinematical age. Based on the $0.565 M_{\odot}$ post-AGB sequence of Schönberner (1983), we can make the following estimate: expansion of the AGB matter with 10 km s^{-1} for 5000 years ($T_{\text{eff}} \simeq 30\,000 \text{ K}$), then formation of the shock and linear increase of its velocity to 40 km s^{-1} for another 1500 years ($T_{\text{eff}} \simeq 38\,000 \text{ K}$). The kinematical age would then be $0.07 \text{ pc} / 40 \text{ km s}^{-1} \times 1.25 \simeq 2100$ years, i.e. smaller than the model's post-AGB age ($\simeq 6500 \text{ yr}$) by a factor of about 3!

Because of the well-known distance to M 15, the mass of the central star can be determined rather precisely: Alves, Bond & Livio (2000) found $M = 0.60 \pm 0.02 M_{\odot}$, a value derived by comparing the observed central-star luminosity with existing post-AGB (core-)mass luminosity relations. However, these authors used a distance to M 15 of 12.3 kpc, and when reduced to 10.2 kpc, a mass of only $0.57 M_{\odot}$ follows. Bianchi et al. (2001) derived directly a mass of $0.62 M_{\odot}$ by combining stellar radius with photospheric gravity, but the error of ($\pm 0.10 M_{\odot}$) is too high as to make this result useful for further applications. Rauch, Heber & Werner (2002) got $M = 0.57_{-0.01}^{+0.02} M_{\odot}$ by means of a NLTE determination of photospheric parameters and a comparison with post-AGB evolutionary tracks in the $T_{\text{eff}}\text{-log } g$ plane.

We conclude that the central star of Ps 1 has a lower mass of only $\simeq 0.57 M_{\odot}$, instead of the $0.60\text{--}0.62 M_{\odot}$ as is usually assumed in the literature where the Alves, Bond & Livio and Bianchi et al. results were taken for granted. With a correction factor of 3 (see above) we estimate the true, i.e. post-AGB age of the nebula to $\simeq 1900 \times 3 \approx 5700$

¹⁸ We note that metal-poor models reach high expansion rates already at rather low stellar temperatures: Figure 10 in Schönberner et al. (2010) shows a PN model with a metallicity reduced by a factor of ten around a central star with $T_{\text{eff}} \simeq 41\,000 \text{ K}$ and a post-shock velocity of already 40 km s^{-1} .

years. This value is consistent with the 6500 years predicted for a $0.565 M_{\odot}$ post-AGB model to reach about 40 000 K (Schönberner 1983) if one considers all the uncertainties concerning the underlying physics like, e.g., post-AGB mass loss history or time of the cessation of the strong AGB wind.

DdDm 1 Otsuka et al. (2009) observed also this object with Subaru/HDS and determined an expansion velocity of $11 \pm 1 \text{ km s}^{-1}$ from, e.g., the split [O III] line (their Table 3). This value corresponds, according to our interpretation, to V_{rim} . A post-shock velocity cannot be derived from these profiles. The 10 %-level velocity is between 25 and 30 km s^{-1} . Nevertheless, a rim velocity of 11 km s^{-1} fits well into the range observed for the other metal-poor objects.

8 Discussion

Based on high-resolution spectrograms of PNe from the Milky Way disk and halo we performed a detailed study on how the expansion properties and internal kinematics of PNe vary with evolution through the HR diagram, i.e. from the young, compact early phase horizontally across the HR diagram and finally down to a stage where the central star is a very hot white dwarf with a comparatively low luminosity.

In particular, we derived, for quite a large sample of objects (23 double-shell, 5 evolved, and 4 metal-poor PNe), accurate expansion velocities of the most conspicuous part of a PN, the rim. Except for the evolved objects, we also determined, for many objects for the first time, the gas velocity at the outer edge of the much fainter, attached shell, i.e. the post-shock velocity, by a method developed earlier by us. The post-shock velocity is important because it is physically connected to the outer shock's propagation which represents the *true* expansion of a PN. The sample investigated here is significantly larger than the ones presented in Paper II and Schönberner et al. (2005b) and comprises objects with different metallicities and evolutionary stages, allowing a meaningful comparison with theory.

The kinematics of planetary nebulae opens the possibility to probe, although only indirectly, the mass-loss history during the final AGB phase (upstream density and post-shock velocity) and the mass-loss evolution during the whole post-AGB stage as well (rim strength and rim expansion). We note explicitly that the very final, high mass-loss phase which removes nearly completely the AGB star's envelope is very brief and thus not directly observable. Also, any variations of the strength of the post-AGB mass loss with stellar temperature, as predicted by, e.g. Pauldrach et al. (2004), is difficult to measure because of the rather high uncertainties involved. The predicted influence of different AGB and post-AGB wind histories on the PN structure (surface brightness) can be seen in Steffen & Schönberner (2006, Figs. 5 and 6 therein).

The existence of a nearly stalling rim during the early evolution of a PN sets also a lower limit to the final mass-

loss rate on the AGB which is necessary to build up sufficient thermal pressure as to decelerate the inner region of the newly formed ionised shell against the pressure of the wind-shocked hot bubble. Based on our hydrodynamical simulations we estimate a lower limit of the final AGB mass-loss rate of the order of $1 \times 10^{-5} M_{\odot} \text{ yr}^{-1}$.

Since our radiation-hydrodynamics simulation were performed without having any detailed comparison with observations in mind and without any fine-tuning, it is not astonishing that none of our model sequences describes all aspects of the PN kinematics quantitatively correct. Taken all simulations together, however, we find a fair and satisfying agreement of computed nebular quantities with their observed counterparts (cf. also Steffen & Schönberner 2006).

From all these evidences discussed here it is clear that the existence of two shell components with distinct properties, such as densities and flow velocities, as seen in nearly all PNe which are in the appropriate evolutionary stage, is just a natural consequence of the prevailing physics and cannot be attributed to two mass loss events with different strengths and velocities, and which are separated in time.

The high post-shock velocities found for the objects of our sample are in big contrast to the canonical “expansion” velocity value of 20–25 km s^{-1} usually used in the literature. The mean post-shock velocity found by us is $\sim 40 \text{ km s}^{-1}$, which corresponds to a true expansion rate of, on the average, $40 \times 1.25 = 50 \text{ km s}^{-1}$, i.e. about twice of the generally adopted value! The reason is that, erroneously, always the peak-to-peak separation of the strongest line profile components were taken as the typical expansion velocity. The mean rim velocity of our sample in Table 1 is 18 km s^{-1} , i.e. close to the canonical value.

In the study on Magellanic Cloud PNe, Dopita et al. (1985) introduced an “expansion” velocity based on the 10 % level of the line profile. This method is much easier to perform, even with data of poorer quality, and yields results much closer to the post-shock velocity. However, the velocity at the 10 % level is, of course, not necessarily equal to the post-shock velocity because it has no physical meaning. Rather this choice is a compromise in the sense of being close to the maximum nebular flow velocity with still sufficient signal above the background. Additionally, the line profile, and the flux at the 10 % level, depends on evolutionary stage, the ion used (cf. Fig. 4), and the spectral resolution.

As example we can use the line profiles of NGC 6826 shown in Fig. 7. The 10 % velocities are 38 km s^{-1} for [N II] and 32 km s^{-1} for [O III], while $V_{\text{post}} = 34 \text{ km s}^{-1}$ (cf. Table 1). Additional examples are provided by the work of Medina et al. (2006) who applied the 10 %-level method as well. For NGC 7009, Medina et al. got $V_{10\%} = 33 \text{ km s}^{-1}$ ([O III]) and 38 km s^{-1} ([N II]), while $V_{\text{post}} = 36 \text{ km s}^{-1}$, and for NGC 6543 $V_{10\%} = 43 \text{ km s}^{-1}$ from both ions, but $V_{\text{post}} = 47 \text{ km s}^{-1}$. Anyway, the 10 % velocities are much closer to V_{post} than the results from the line-peak separa-

tion which are for the three objects 8, 16, and 18 km s⁻¹, respectively (see Table 1).

In this context we warn the reader to put too much confidence into any kinematical age determination of a PN and to use this value for making quantitative statements on, e.g., central-star masses. Even with a precise value of an “expansion” velocity and proper nebular radius, a correction must be applied that accounts for the difference between measured and true expansion velocity and its acceleration during the past. Due to the complex hydrodynamical processes involved, this correction is rather uncertain and depends as well on the evolutionary state. Without such a correction, any determination of a post-AGB age from the nebular size and expansion is completely useless.

We could not detect any significant deceleration of nebular matter during the evolution around maximum stellar temperature and down to low stellar luminosities, as recently reported by Pereyra et al. (2013). However, the number of objects investigated here is too small as to make a firm conclusion on this matter. We only remark that nebulae in such phase are prone to ionisation stratification, making any velocity measurements ion-dependent! The numerous PNe which do not recombine because they have more slowly evolving nuclei will certainly not decelerate their expansion if the nucleus fades.

Finally, we repeat that all statements made in this study refer to the expansion properties of PNe with central stars of normal surface composition only. Nebula around Wolf-Rayet central stars have a faster expanding rim, obviously because of the much stronger stellar wind (cf. Medina et al. 2006). It is expected that the expansion properties of PNe with a Wolf-Rayet central star, if coupled to hydrodynamical simulations, could establish very useful constraints for Wolf-Rayet winds. However, because the formation mechanism and the evolution of hydrogen-deficient post-AGB stars are not known to date, hydrodynamic simulations are impossible.

9 Results and conclusion

The results of our study are in line with the prediction of radiation-hydrodynamic simulations in that the interaction of the fast central-star wind with the slow AGB wind via a hot bubble of shock-heated wind gas is not the main driving agent of a PN: At the beginning of the post-AGB evolution and during the late evolution with a faint central star the wind power is just sufficient to avoid the collapse of the PN towards the star. Only during the middle of the nebular evolution, if the wind power increases to its maximum (cf. Fig. 2, middle panel), the winds interaction gets important and forms the conspicuous nebular rims. But even then most of the nebular mass is still contained in the less prominent shells, and the expansion speed of their leading shocks is not influenced at all by the stellar wind.

Our main results/conclusions are as follows:

- There exists a rather tight correlation of the internal kinematics with age/stellar temperature which, however, is distinct between rim and shell. The shell’s leading shock accelerates from the AGB wind speed of $\simeq 10$ km s⁻¹ to about 50 km s⁻¹ ($V_{\text{post}} \simeq 40$ km s⁻¹), first as a D-type ionisation front and then in a “champagne”-flow configuration, because (i) the electron temperature increases in line with the growing energy of the ionising photons, and (ii) the density gradient of the halo may steepen with distance from the star. The rim, on the other hand, is driven by the stellar wind power which increases as the star shrinks. For young objects the rim matter expands even *slower* than the former AGB wind, but at the end of the horizontal evolution values of about 30 km s⁻¹ are reached.
- Since both rim and shell obviously expand outwards independently of each other, the expansion of a PN is by no means ballistic. Rather, *the whole PN is a dynamical system throughout its entire evolution, without reaching a self-similar stage of expansion at any time.*
- The difference between rim expansion and post-shock velocity *decreases* with progress of evolution from about 25 km s⁻¹ for the youngest objects till about 15 km s⁻¹ for the most evolved objects of our sample.
- The high expansion velocities of the outer shock indicate a steep gradient in the radial upstream density profile, i.e. in the halo, which is only possible if the mass loss during the final AGB evolution “accelerates” continuously. This may be an indication that in the normal case the PN precursor left the tip of the AGB quite soon after the last thermal pulse on the AGB, i.e. during recovering from the pulse. The only exception in our sample is NGC 2022 whose unusual low post-shock velocity hints to a period of constant final AGB mass-loss rate.
- The line profiles of four targets with intrinsically faint but very hot central stars could be interpreted in terms of a reionisation process after a rather severe but short recombination phase caused by the rapid luminosity drop of the star. We found in all cases quite high flow velocities of 40–50 km s⁻¹ at the outer edge of the newly created reionised shell which are comparable to those measured for objects which are still in the high-luminosity phase of their evolution.
- The expansion behaviour of the four metal-poor objects is as expected from theory: Compared to objects with normal (i.e. Galactic disk) metallicity, post-shock velocities are generally higher because of the higher electron temperature, and rim velocities lower because of the weaker winds interaction.

To summarise up, our study demonstrates, in line with our previous ones, that the expansion of a PN is much faster than assumed so far. The reason is an incorrect assignment of a measured velocity, usually that of the most conspicuous part of the nebulae (i.e. the rim), to be the “expansion velocity” of a PN. Instead, it is the outer shell’s shock whose propagation determines the true expansion of a PN. The only

velocity which is physically related to the shock expansion is the gas velocity immediately behind the shock, the post-shock velocity. But this velocity is, in general, higher than the velocity measured for the rim by factors up to about 7 for very young objects.

In closing we state that the *expansion velocities of PNE quoted in the literature and frequently used in statistical studies must be treated with utmost care. It is absolutely necessary to check which kind of velocity is measured and how this velocity refers to the real expansion velocity of the object in question.*

Acknowledgements. We are grateful to the referee for his careful reading of the manuscript and the very short reviewing time. C.S. acknowledges support by DFG grant SCHO 394/26.

References

- Aller, L.H., & Keyes, C.D. 1987, ApJS, 65, 405
 Alves, D.R., Bond, H.E., & Livio, M. 2000, AJ, 120, 2044
 Bianchi, L. 1992, A&A, 260, 314
 Bianchi, L., Bohlin, R., Catanzaro, G., Ford, H., & Manchado, A. 2001, AJ, 1538
 Blöcker, T. 1995, A&A, 299, 755
 Blöcker, T., & Schönberner, D. 1997, A&A, 324, 991
 Bohuski, T.J., & Smith, M.G. 1974, ApJ, 193, 197
 Chevalier, R.A.: 1997, ApJ 488, 263
 Chu Y.-H. 1989, in Planetary Nebulae, ed. S. Torres-Peimbert, IAU Symp. No. 131, 105
 Chu Y.-H., Jacoby G.H., & Arendt R. 1987, ApJS, 64, 529
 Chu Y.-H., Kwitter K.B., Kaler J.B., & Jacoby G.H. 1984, PASP, 96, 598
 Contreras, M.E., Vázquez, R., Miranda, L.F., et al. 2010, AJ, 139, 1426
 Corradi, R.L.M., Schönberner, D., Steffen, M., & Perinotto, M. 2000, A&A, 354, 1071 (Paper I)
 Corradi, R.L.M., Steffen, M., Schönberner, D., & Perinotto, M.: 2003, in Planetary Nebulae, Their Evolution and Role in the Universe, ed. S. Kwok, M. Dopita, & R. Sutherland, IAU Symp. No. 209, 455
 Corradi, R.L.M., Schönberner, D., Steffen, M., & Perinotto, M. 2003, MNRAS, 340, 417
 Corradi, R.L.M., Steffen, M., Schönberner, D., & Jacob, R. 2007, A&A, 474, 529 (Paper II)
 Dalnodar, S. 2012, in Planetary Nebulae: An Eye to the Future, eds. A. Manchado, L. Stanghellini, & D. Schönberner, IAU Symp. No. 283, 338
 Dopita, M.A., & Meatheringham, S.J. 1991, ApJ, 367, 115
 Dopita, M.A., Ford, H.C., Lawrence, C.J., & Webster, B.L. 1985, ApJ, 296, 390
 Flannery, B.A., & Herbig, G.H. 1973, ApJ, 183, 491
 Franco, J., Tenorio-Tagle, G., & Bodenheimer, P. 1990, ApJ, 349, 126
 Frank, A., Balick, B., & Riley, J. 1990, AJ, 106, 1903
 Frew, D.J., Bojičić, I.S., & Parker, Q.A. 2012, in Planetary Nebulae: An Eye to the Future, eds. A. Manchado, L. Stanghellini, & D. Schönberner, IAU Symp. No. 283, 362
 Georgiev, L.N., Peimbert, M., Hillier, D.J., et al. 2008, ApJ, 681, 333
 Gesicki, K., & Zijlstra, A.A. 2000, A&A 358, 1058
 Gesicki, K., Acker, A., Szczerba, R.: 1996, A&A, 309, 907
 Gesicki, K., Zijlstra, A.A., Acker, A., & Szczerba, R. 1998, A&A, 329, 265
 Gesicki, K., Acker, A., & Zijlstra, A.A. 2003, A&A, 400, 957
 Gesicki, K., Zijlstra, A.A., Szyska, C., et al. 2010, A&A, 514, A54
 Guerrero, M.A., Villaver, E., & Manchado, A. 1998, ApJ, 507, 889
 Guerrero, M.A., Manchado, A., Stanghellini, L., & Herrero, A. 1996, ApJ, 464, 847
 Guerrero, M.A., Ramos-Larios, G., & Massa, D.: 2010, PASA, 27, 210
 Heber, U., Dreizler, S., & Werner, K. 1993, Acta Astron., 43, 337
 Henry, R.B.C., Kwitter, K.B., & Balick, B. 2004, AJ, 127, 2284
 Howard, J.W., Henry, R.B.C., & McCartney, S. 1997, MNRAS, 284, 465
 Jacob, R., Schönberner, D., & Steffen, M. 2013, A&A, 558, A78
 Jacob, R., Schönberner, D., Lehmann, H., et al. Planetary Nebulae: An Eye to the Future, eds. A. Manchado, L. Stanghellini, & D. Schönberner, IAU Symp. No. 283, 400
 Jeffery, C.S., & Schönberner, D. 2006, A&A, 459, 885
 Koo, B.-C., & McKee, C.F. 1992, ApJ, 388, 103
 Malkov, Y.F. 1997, Astronomy Reports 41, 760
 Marcolino, W.L.F., Hillier, D.J., de Araujo, F.X., & Pereira, C.B. 2007, ApJ, 654, 1068
 Marten, H., & Schönberner, D. 1991, A&A, 248, 590
 Marten, H., & Szczerba, R. 1997, A&A, 325, 1132
 McCarthy, J.K., Méndez, R.H., & Kudritzki, R.-P. 1997, in Planetary Nebulae, eds. H.J. Habing, & H.J.G.L.M. Lamers, IAU Symp. No. 180, 120
 McNamara, B.J., Harrison, T.E., & Baumgardt, H. 2004, ApJ, 602, 264
 Medina, S., Peña, M., Morisset, C., & Stasińska, G.: 2006, Rev. Mexicana Astron. Astrofis., 42, 53
 Mellema, G. 1994, A&A, 290, 915
 Mellema, G. 1995, MNRAS, 277, 173
 Mellema, G. 2004, A&A, 416, 623
 Méndez, R.H., Kudritzki, R.-P., Herrero, A., Husfeld, D., & Groth, H.G. 1988, A&A, 190, 113
 Méndez, R.H., Kudritzki, R.-P., & Herrero, A. 1992, A&A. 260, 329
 Miszalski, B., Mikolajewskaja, J., Köppen, J., et al. 2011, A&A, 528, A39
 Moe, M., & de Marco, O. 2006, ApJ, 650, 916
 Morisset, C., & Georgiev, L. 2009, A&A, 507, 1517
 Neiner, C., Acker, A., Gesicki, K., & Szczerba, R. 2000, A&A, 358, 321
 Otsuka, M., Hyung, S., Lee, S.-J., Izumiura, H., & Tajitsu, A. 2009, ApJ, 705, 509
 Otsuka, M., Tajitsu, A., Hyung, S., & Izumiura, H. 2010 ApJ, 723, 658
 Patriarchi, P., & Perinotto, M. 1991, A&AS, 91, 325
 Pauldrach, A.W.A., Hoffmann, T.L., & Méndez, R.H. 2004, A&A, 419, 1111
 Pauldrach, A.W.A., Puls, J., Kudritzki, R.-P., Méndez, R.H., & Heap, S.H. 1988, A&A, 207, 123
 Pereyra, M., Richer, M.G., & López, J.A. 2013, ApJ, 771, A2
 Perinotto, M., Kifonidis, K., Schönberner, D., & Marten, H. 1998, A&A, 332, 1044
 Perinotto, M., Schönberner, D., Steffen, M., & Calonaci, C. 2004, A&A, 414, 993
 Plait, P., & Soker, N. 1990, AJ, 99, 1883
 Pottasch, S.R., & Bernard-Salas, J. 2010, A&A, 517, A95
 Ramos-Larios, G., Vázquez, R., Guerrero, M.A., et al. 2012, MNRAS, 423, 3753
 Rauch, T., Heber, U., & Werner, K. 2002, A&A, 381, 1007

- Rauch, T., Köppen, J., Napiwotzki, R., & Werner, K. 1999, *A&A*, 347, 169
- Reimers, D. 1975, in *Problems in Stellar Atmospheres and Envelopes*, eds. B. Baschek, W.H. Kegel, & G. Traving, Springer (Berlin), 229
- Richer, M.G., López, J.A., Pereyra, M., et al. 2008, *ApJ*, 689, 203
- Richer, M.G., López, J.A., García-Díaz, M.T., Clark, D.M., & Pereyra, M. 2010, *ApJ*, 716, 857
- Robinson, G.J., Reay, N.K., & Atherton, P.D. 1982, *MNRAS*, 199, 649
- Sabbadin F., Bianchini, A., & Hamzaoglu, E. 1984, *A&A*, 136, 193
- Sabbadin F., Turatto, M., Cappellaro, E., Benetti, S., & Ragazzoni, R. 2004, *A&A*, 416, 955
- Sandin, C., Schönberner, D., Roth, M.M., et al. 2008, *A&A*, 486, 545
- Schmidt-Voigt, M., & Köppen, J., 1987a, *A&A*, 174, 211
- Schmidt-Voigt, M., & Köppen, J., 1987b, *A&A*, 174, 223
- Schönberner, D. 1983, *ApJ*, 272, 708
- Schönberner, D., Jacob, R., & Steffen, M. 2005a, *A&A*, 441, 573
- Schönberner, D., Jacob, R., Steffen, M., et al. 2005b, *A&A*, 431, 963
- Schönberner, D., Steffen, M., & Jacob, R. 2004, in *Asymmetric Planetary Nebulae III*, eds. M. Meixner, J. Kastner, & N. Soker, ASP Con. Ser. 313, 283
- Schönberner, D., Jacob, R., Sandin, C., & Steffen, M. 2010, *A&A*, 523, A86
- Shu, F. H., Lizano, S., Galli, D., Cantó, J., & Laughlin, G. 2002, *ApJ*, 580, 969
- Stanghellini, L., & Pasquali, A. 1995, *ApJ*, 452, 286
- Steffen, M., & Schönberner, D. 2006, in *Planetary Nebulae in our Galaxy and Beyond*, eds. M.J. Barlow & R.H. Méndez, IAU Symp. No. 234, 285
- Steffen, M., Szczerba, R., & Schönberner, D. 1998, *A&A*, 337, 149
- Steffen, W., & López, J. A. 2006, *Rev. Mexicana Astron. Astrofis.*, 42, 99
- Steffen, W., García-Segura, G., & Koning, N. 2009, *ApJ*, 691, 696
- Tajitsu, A., & Otsuka, M. 2006, in *Planetary Nebulae in our Galaxy and Beyond*, eds. M.J. Barlow & R.H. Méndez, IAU Symp. No. 234, 523
- Tenorio-Tagle, G 1979, *A&A*, 71, 59
- Tylenda, R. 1986, *A&A*, 156, 217
- van den Bosch, R., de Zeeuw, T., Gebhardt, K., Noyola, E., & van de Ven, G. 2006, *ApJ*, 641, 852
- Villaver, E., Machado, A., & García-Segura, G. 2002, *ApJ*, 581, 1204
- Weinberger R. 1989, *A&AS*, 78, 301
- Wilson O.C. 1950, *ApJ*, 111, 279

A Compilation of line profiles and velocity data

The finally extracted line profiles of 17 objects are collected in Fig. A1. In cases of multiple observations, only one has been selected. The individual velocities V_{rim} and V_{post} based on the strong [O III] and [N II] lines of our target objects are compiled in Table A1. Data for $H\alpha$ are not given because shell and rim are rarely resolved. For comparison, the last two columns give values from the literature.

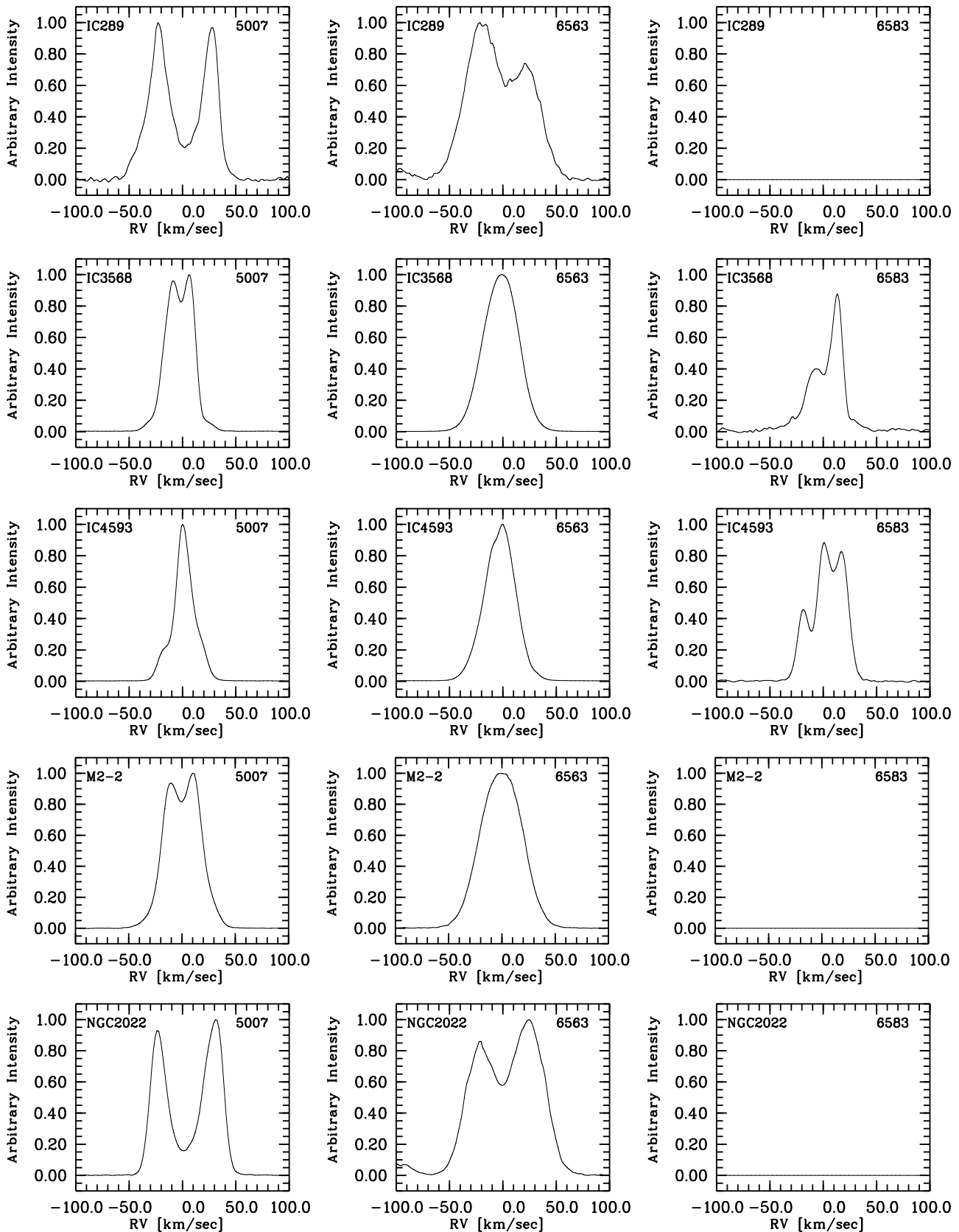


Fig. A1 Normalised, central line-of-sight emission line profiles of $[O\text{ III}]\lambda 5007\text{ \AA}$, $H\alpha$, and $[N\text{ II}]\lambda 6583\text{ \AA}$. Empty panels: line not observed.

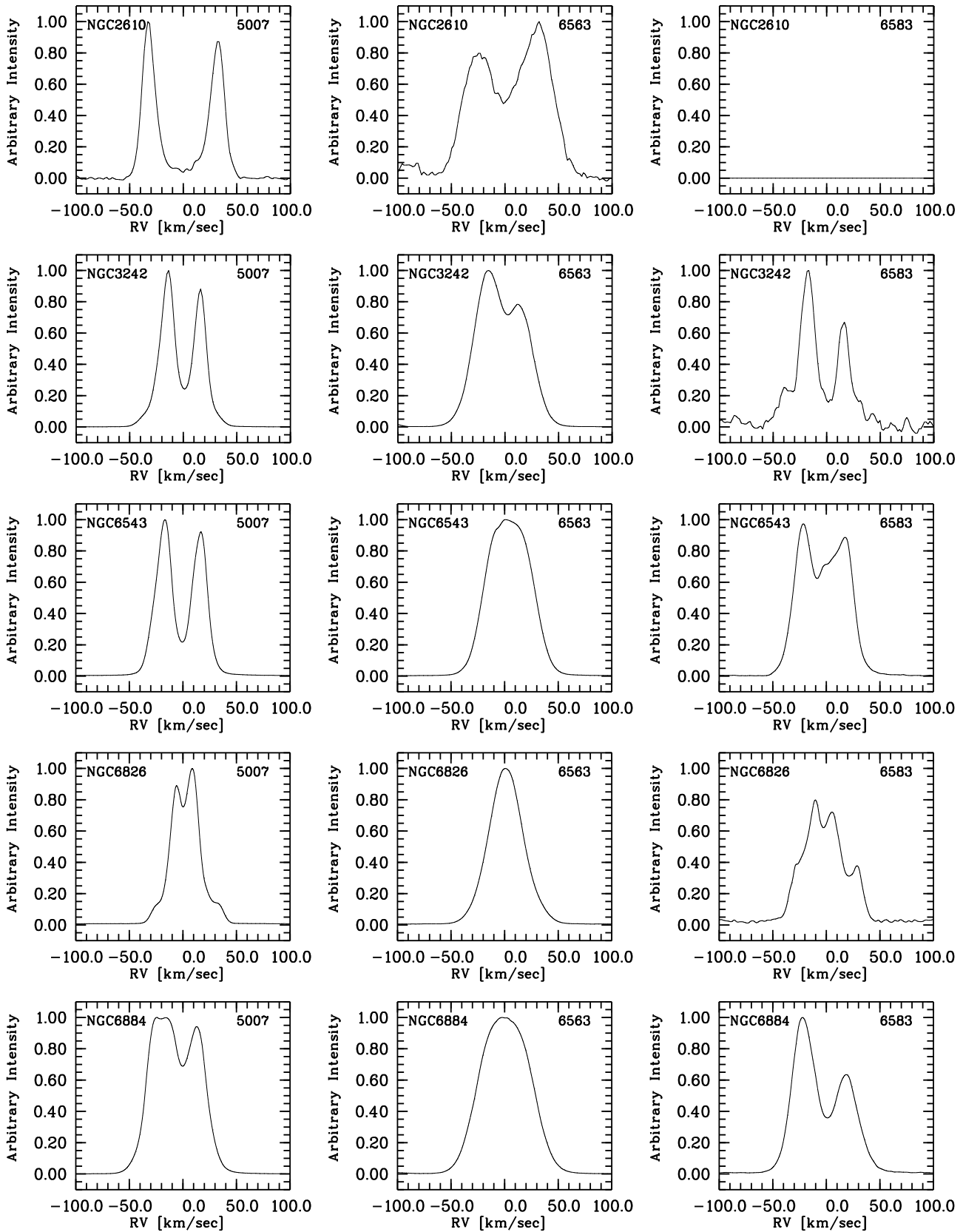


Fig. A1 Figure A1 continued.

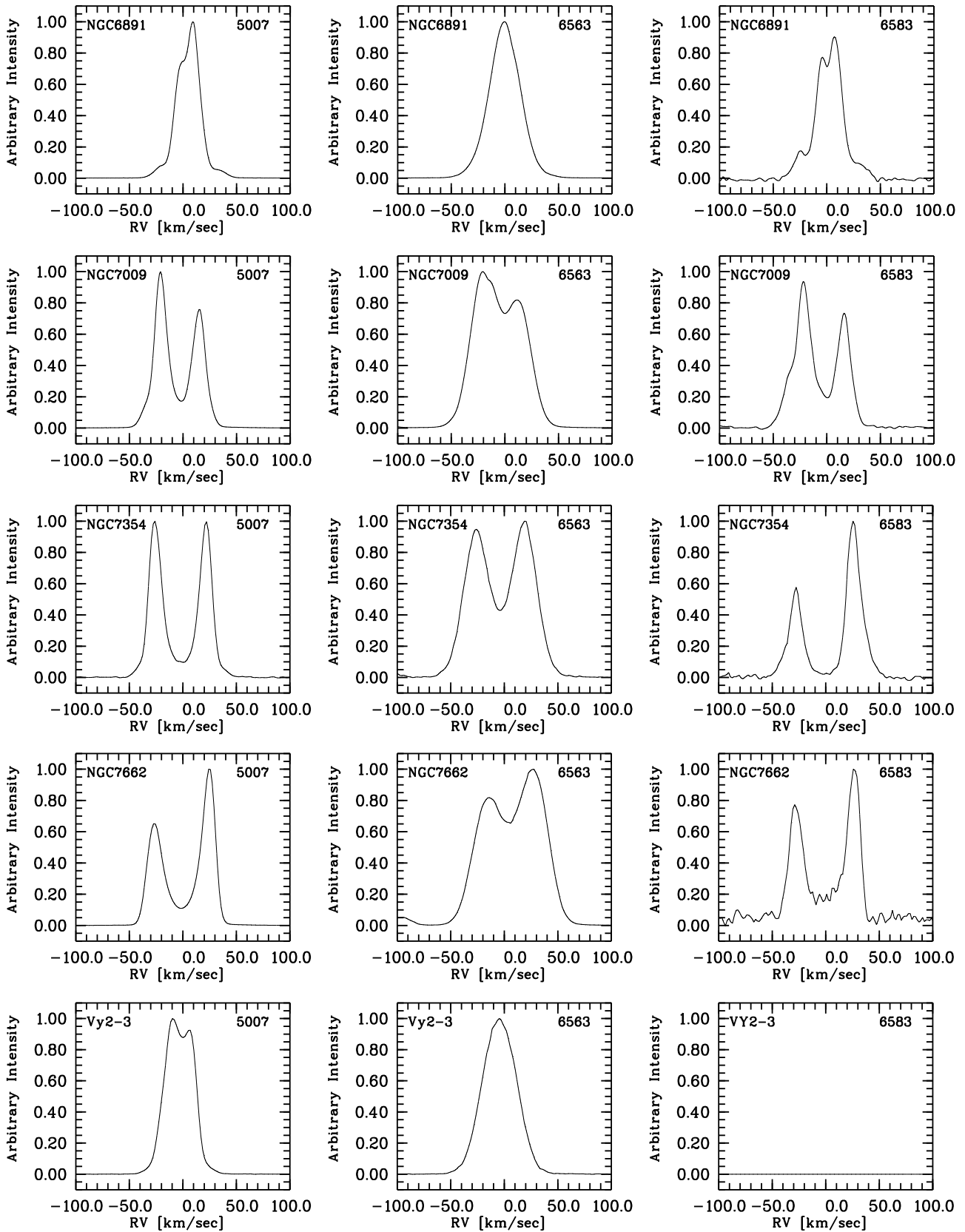


Fig. A1 Figure A1 continued.

Table A1 Individual velocity measurements for rims and shells from central [O III] $\lambda\lambda$ 4959, 5007 Å and [N II] $\lambda\lambda$ 6548, 6583 Å emission lines based on Tautenburg échelle spectrogrammes of PNe in their high central-star luminosity evolutionary stage. Rim velocities (V_{rim}) are from the peak separations of the two innermost Gaussians fitted to the strong line profile components, while shell velocities (V_{post}) refer to the separations of the extremes of the line profile derivatives (or sigmas of shell Gaussians) at the line wings/shoulders as described in Sect. 2.

Object	V_{rim} (km s ⁻¹)				V_{post} (km s ⁻¹)				Literature ^a	
	4959 Å	5007 Å	6548 Å	6583 Å	4959 Å	5007 Å	6548 Å	6583 Å	[O III]	[N II]
IC 289	25.7	25.8	–	–	–	43.2	–	–	22, 27	–
	–	25.2	–	–	–	–	–	–	–	–
	25.2	24.9	–	–	–	50.7	–	–	–	–
	26.1	25.3	–	–	–	45.5	–	–	–	–
IC 3568	–	–	9.3	9.6	–	–	–	30.6	8 ²	–
	8.1	8.3	–	–	33.5	33.2	–	–	–	–
	9.3	9.3	–	–	33.2	32.8	–	–	–	–
IC 4593	–	–	4.5	7 ^b	–	–	23.3	24.2	8 ³ , 12 ³	–
	–	–	3.5	7 ^b	–	–	24.6	23.8	–	–
	3.1	3.6	–	–	22.0	22.8	–	–	–	–
M 2-2	11.1	11.3	–	–	33.4	37.4	–	–	–	17 ⁶
	11.6	11.6	–	–	36.9	35.1	–	–	–	–
	10.9	11.0	–	–	34.0	37.6	–	–	–	–
	11.2	11.0	–	11.0	37.6	37.4	–	–	–	–
NGC 2022	28.7	28.9	–	–	–	–	–	–	29 ⁴ , 27 ⁵	–
	29.2	29.1	–	–	–	–	–	–	–	–
NGC 2610	32.6	32.0	–	–	–	–	–	–	–	–
	32.3	32.5	–	–	–	–	–	–	14, 34	–
NGC 3242	15.7	15.9	17.2	18.0	38.3	39.1	–	–	19.5 ⁵ , 35.7 ⁵	19.7 ⁵
	16.6	16.6	–	18.4	40.3	40.0	–	–	–	–
	15.2	15.3	–	17.5	37.2	37.5	–	40.3	–	–
	14.9	15.0	–	17.1	37.9	38.4	–	38.9	–	–
NGC 6543	–	–	20.5	20.8	–	–	44.0	45.6	19.5, 43 ⁷	20, 43 ⁷
	16.3	16.5	–	–	–	–	–	–	–	–
NGC 6826	–	–	8.9	8.6	–	–	33.9	33.7	–	10.6 ⁶ , 28.3 ⁶
	–	–	8.6	8.2	–	–	33.1	33.7	–	–
	7.6	7.6	–	–	32.8	33.1	–	–	–	–
	7.8	7.8	–	–	31.5	32.6	–	–	–	–
NGC 6884	–	–	18.9	19.4	–	–	–	–	23	24.0 ⁶
NGC 6891	–	–	7.5	6.7	–	–	32.3	34.4	7	9.7 ⁶ , 30 ⁶
	–	–	7.3	6.8	–	–	34.4	34.0	–	–
	6.6	6.6	–	–	31.0	31.7	–	–	–	–
NGC 7009	–	–	18.4	18.6	–	–	38.3	35.4	20, 33 ⁷	20, 38 ⁷
	17.8	17.8	–	–	35.9	36.1	–	–	–	–
NGC 7354	–	–	27.2	27.2	–	–	45.7	45.6	25	28 ⁸ , 35 ⁸
	23.8	23.8	–	27.6	–	44.2	–	–	–	–
	23.6	24.0	–	26.5	–	–	–	46.1	–	–
	24.4	24.2	27.7	26.3	43.8	46.9	–	–	–	–
	23.5	23.7	26.9	26.8	–	–	42.7	46.3	–	–
NGC 7662	–	–	26.9	26.7	–	–	–	–	26.1 ⁵	25.4 ⁶
	25.5	25.7	28.1	28.1	–	–	–	–	–	–
Vy 2-3	8.8	8.7	–	–	34.9	34.6	–	–	16, 12	13.0 ⁶
	8.7	8.7	–	–	34.6	35.4	–	–	–	–

Notes: Uncertain measurements are rounded to full km s⁻¹. ^a If not noted otherwise, from Weinberger (1989) which incorporates all the previous references. ^b From half width at half maximum of the central Gauss profile.

¹ Flannery & Herbig (1973). ² The [O III] line profile presented in Gesicki et al. (1996) shows weak wings similar to our observation, indicating a comparatively high shell velocity (Tab. A1). ³ From Weinberger (1989), but for H α ; ⁴ Sabbadin, Bianchini & Hamzaoglu (1984); ⁵ Schönberner et al. (2005b); ⁶ Guerrero et al. (1998); ⁷ $V_{10\%}$ velocity from Medina et al. (2006); ⁸ Contreras et al. (2010).